

## Fully developed viscous and viscoelastic flows in curved pipes

By YURUN FAN<sup>1,3</sup>, ROGER I. TANNER<sup>1</sup>  
AND NHAN PHAN-THIEN<sup>2</sup>

<sup>1</sup>Department of Mechanical & Mechatronic Engineering, The University of Sydney,  
NSW 2006, Australia

<sup>2</sup>Department of Mechanical Engineering, National University of Singapore, Singapore 119260

<sup>3</sup>State Key Laboratory of Fluid Power Control and Transmission, Zhejiang University,  
310027 China

(Received 10 December 1999 and in revised form 12 February 2001)

Some  $h$ - $p$  finite element computations have been carried out to obtain solutions for fully developed laminar flows in curved pipes with curvature ratios from 0.001 to 0.5. An Oldroyd-3-constant model is used to represent the viscoelastic fluid, which includes the upper-convected Maxwell (UCM) model and the Oldroyd-B model as special cases. With this model we can examine separately the effects of the fluid inertia, and the first and second normal-stress differences. From analysis of the global torque and force balances, three criteria are proposed for this problem to estimate the errors in the computations. Moreover, the finite element solutions are accurately confirmed by the perturbation solutions of Robertson & Muller (1996) in the cases of small Reynolds/Deborah numbers.

Our numerical solutions and an order-of-magnitude analysis of the governing equations elucidate the mechanism of the secondary flow in the absence of second normal-stress difference. For Newtonian flow, the pressure gradient near the wall region is the driving force for the secondary flow; for creeping viscoelastic flow, the combination of large axial normal stress with streamline curvature, the so-called hoop stress near the wall, promotes a secondary flow in the same direction as the inertial secondary flow, despite the adverse pressure gradient there; in the case of inertial viscoelastic flow, both the larger axial normal stress and the smaller inertia near the wall promote the secondary flow.

For both Newtonian and viscoelastic fluids the secondary volumetric fluxes per unit of work consumption and per unit of axial volumetric flux first increase then decrease as the Reynolds/Deborah number increases; this behaviour should be of interest in engineering applications.

Typical negative values of second normal-stress difference can drastically suppress the secondary flow and in the case of small curvature ratios, make the flow approximate the corresponding Poiseuille flow in a straight pipe. The viscoelasticity of Oldroyd-B fluid causes drag enhancement compared to Newtonian flow. Adding a typical negative second normal-stress difference produces large drag reductions for a small curvature ratio  $\delta = 0.01$ ; however, for a large curvature ratio  $\delta = 0.2$ , although the secondary flows are also drastically attenuated by the second normal-stress difference, the flow resistance remains considerably higher than in Newtonian flow.

It was observed that for the UCM and Oldroyd-B models, the limiting Deborah numbers met in our steady solution calculations obey the same scaling criterion as proposed by McKinley *et al.* (1996) for elastic instabilities; we present an intriguing

problem on the relation between the Newton iteration for steady solutions and the linear stability analyses.

---

## 1. Introduction

The motion of fluids through curved pipes driven by a pressure drop is a fundamental and much-studied problem. The practical importance of such flows in engineering (hydraulic pipe systems, heat exchange devices, etc.) and in biomechanics (e.g. blood flow) is evident, as comprehensively reviewed by Berger, Talbot & Yao (1983). Due to fluid inertia, secondary flow appears whenever fluid flows in curved pipes. In the limiting case of small curvature ratio,  $\delta = a/R$ , where  $a$ ,  $R$  are the radii of the tube and the coil respectively (see figure 1), and ignoring all terms arising due to the coil curvature except centripetal acceleration terms, the governing equations can be reduced and solved in a stream-function/vorticity form (Dean 1927, 1928). Thus a single parameter, the Dean number, which is a Reynolds number modified by the curvature ratio, determines the flow resistance (the drag) and the character of the secondary flow. Roughly speaking, these perturbation solutions are valid when  $\delta < 0.01$ . An exception is the perturbation solution of Topakoglu (1967) which does not invoke Dean's approximation but is limited to small Reynolds numbers. Austin & Seader (1973) obtained finite difference solutions with curvature ratio as large as 0.2; Nunge & Lin (1973) investigated the large curvature ratio effect by using a Fourier series method for small Dean numbers and the boundary layer approximation of Ito (1969) for large Dean numbers, but they were somewhat frustrated in attempting to join these two solutions smoothly; Nandakumar & Masliyah (1982) presented some finite difference solutions for  $\delta = 0.1$ ; Soh & Berger (1987) solved the full Navier–Stokes equation from  $\delta = 0.01$  to  $\delta = 0.2$  using a finite difference method; they found that the  $\delta$ -dependence of the flow resistance increases as the Dean number increases.

In practical applications, a large curvature ratio is often desirable, for instance to increase the heat or mass exchange. The present investigation was partly motivated by the work of Jones, Thomas & Aref (1989) on chaotic mixing in a twisted pipe consisting of piecewise curved tubes. Using standard dynamical system diagnostics and Dean's perturbation solution they demonstrated that through an appropriate arrangement of the pitch angles, the steady, laminar flow in the twisted pipe can produce chaotic particle advection that enhances the mixing quality considerably. To study advective mixing, accurate velocity fields are necessary, especially for the chaotic mixing process in which the fluid elements are stretched exponentially with time; as a consequence, errors in the numerical velocity field will be convected with fluid particles, accumulated along particle trajectories, and later grow exponentially with time (Souvaliotis, Jana & Ottino 1995). In this study one of our intentions is to obtain accurate numerical solutions for fully developed, incompressible, laminar flows in curved pipes with arbitrary curvature ratios. Earlier numerical simulations on curved pipe flow are based on checking solutions with the perturbation solutions and, in the high Dean number region, comparison with the previously published data. To make the error estimation more solidly grounded, we propose three criteria based on the global torque- and momentum-balance requirements; as these criteria check not only the velocity field but also the velocity gradient and the extra stress fields, they can be used by subsequent investigators.

It is rather surprising to find that, despite its important applications, the flow of

viscoelastic fluids in curved pipes has received much less attention in the literature than its Newtonian counterpart. Jones & Davies (1976) investigated dilute aqueous solutions of macromolecules in curved tubes, and their experiments showed that minute amounts of solute could produce significant delayed departure of the flow rate from Poiseuille flow, a phenomenon named *drag reduction* in the laminar region. In Mashelkar & Devarajan (1976), the shear-thinning effect on the frictional loss was carefully measured and formulated using the boundary-layer approximation; their study showed that the departure from the Poiseuille flow rate occurs at practically the same value of Reynolds number for Newtonian and purely viscous non-Newtonian fluids, whereas such a departure occurs at progressively higher Reynolds numbers for viscoelastic fluids as the polymer concentration increases. Some researchers simply attributed the laminar drag reduction to attenuation of the secondary flow, though there was no experimental evidence. For example, Tsang & James (1980) tried to explain the drag reduction by estimating the cross-sectional stresses based on Dean's solution and several molecular models but ignored the axial normal stress. By considering a viscoelastic constitutive equation similar to the Oldroyd-B model, Thomas & Walters (1963) obtained a perturbation expression for the flow rate in the regime of small curvature ratios. This work was later extended by Bowen, Davies & Walters (1991) to a perturbation solution for the creeping flow of an upper-convected Maxwell (UCM) fluid without invoking Dean's approximation. More recently, Robertson & Muller (1996) presented a perturbation solution for Oldroyd-B fluid with inertia, which contains UCM fluid as a limiting case. Although these perturbation solutions are limited by small inertial or elastic levels, they are valuable for checking numerical solutions. These perturbation solutions indicate that fluid viscoelasticity promotes a secondary flow in the same direction as the inertial secondary flow and, as the elastic level increases, there is a short period of drag reduction (extremely small) followed by drag enhancement.

The mechanism of the laminar drag reduction and secondary flow caused by viscoelasticity is still not well understood, especially with the parameters outside the perturbation window. One of our primary goals is to characterize the viscoelastic effects on the flow resistance and the secondary flow in curved pipes within a large range of the curvature ratio. To reduce the complexity of the problem, we shall concentrate on a constant-viscosity Oldroyd-3-constant model proposed by Phan-Thien & Huilgol (1985), which includes the UCM model, and the Oldroyd-B model as special cases. With this model, we can examine the effects of the fluid inertia, the first and second normal-stress differences and their interactions, without the complexities caused by shear-thinning viscosity. We hope the study will shed light on the mechanism of the secondary flow caused by viscoelasticity and reveal the complex dependence of the flow resistance on the secondary flow, as well as on the curvature ratio.

For curvilinear flows, another important research realm is to predict the flow transitions and instabilities. For Newtonian fluids, the onset and development of bifurcation of the secondary flows at high Dean numbers in a curved pipe with small curvature ratio was discovered and studied numerically by Daskopoulos & Lenhoff (1989), Dennis & Ng (1982), Dennis & Riley (1991) and Yanase, Goto & Yamamoto (1989). The destabilizing effects of viscoelasticity on the steady flow of polymer melts and solutions were well documented, and over the past ten years, significant experimental and theoretical progress has been made in elucidating the mechanisms of the particular class of fluid dynamic instabilities termed 'purely elastic', i.e. the instabilities in the absence of inertia. A comprehensive review of the literature has been provided by Shaqfeh (1996). A central conclusion from the recent work is that

the destabilizing mechanism leading to purely elastic instabilities is the combination of streamline curvature and large elastic normal stresses which give rise to a tension along the fluid streamlines, the so-called hoop stresses. McKinley, Pakdel & Oztekin (1996) proposed a dimensionless criterion that can be used to characterize and unify the critical condition required for onset of purely elastic instabilities in a wide range of different flow geometries; the scaling incorporates both the elastic (first) normal-stress difference in the flow direction and the magnitude of the streamline curvature. The criterion, however, does not apply to the cases where the second normal stress difference is non-zero, which proves to have large influence on the flow stability. Beris, Avgousti & Souvaliotis (1992) indicated that the major effect of the negative second normal stress difference is to suppress viscoelastic instabilities.

Graham (1998) studied the effect of superimposing axial flows on Taylor–Couette flows of UCM and Oldroyd-B fluids; his analysis predicts that the addition of a relatively weak axial flow can significantly enhance the stability of the azimuthal Couette flow. The stabilization is due to the axial (tensile) stress introduced by the axial flow, which resists (or overshadows) the destabilizing hoop stress. Note that the situation here is to create a negative second normal stress difference for the azimuthal Couette flow by the positive first normal stress difference of an axial shear flow. For viscoelastic flows in curved pipes, as far as we are aware, owing to the lack of analytic base-flow solutions, no one has pursued in depth the instability problem. In the present study we only seek laminar, steady solutions in curved pipes, which may provide the base solutions for possible future elastic instability investigations. Furthermore, we shall find some subtle relations between our steady solution computation and flow stability analyses. For example, the hoop stress in the main flow destabilizes the flow by initially producing a secondary flow which will give rise to a tensile stress in the neutral direction; this tensile stress, however, tends to stabilize the main flow, i.e. to weaken the secondary flow.

We use the  $h$ - $p$  finite element method which is well known for its flexible local enrichment of the interpolation order and the exponential convergency towards the accurate solution for smooth problems. The Navier–Stokes equation is solved in the velocity/pressure formulation and the solutions can be checked by the published data. For the viscoelastic flow, six additional stress components are solved for with the constitutive equations, in which some special techniques developed for viscoelastic flows are employed. The finite element solutions are validated through comparing with the perturbation solutions of Robertson & Muller (1996) and further confirmed by the three criteria mentioned earlier. More accurate solutions can be obtained through increasing the interpolation orders (the  $h$ - $p$  extension). In sequence, we shall study Newtonian flow, the creeping flow of UCM fluid and the inertial flow of Oldroyd-B fluid. The impact of the non-zero second normal stress on the flow resistance and secondary flow is examined, in which the relation of the drag reduction/enhancement to the attenuation of the secondary flow is discussed for large and small curvature ratios.

## 2. Basic equations and perturbation solutions

The momentum and continuity equations for incompressible, steady flows are

$$\rho(\mathbf{u}^* \cdot \nabla)\mathbf{u}^* = -\nabla P^* + \nabla \cdot \boldsymbol{\tau}^*, \quad (2.1)$$

$$\nabla \cdot \mathbf{u}^* = 0, \quad (2.2)$$

where  $\mathbf{u}^*$  is the velocity,  $\rho$  the density, and  $P^*$ ,  $\boldsymbol{\tau}^*$  are the pressure and the extra stress, respectively. The constitutive equation for viscoelastic fluids considered in this study is the Oldroyd-3-constant model proposed by Phan-Thien & Huilgol (1985) in which the extra stress consists of two parts:  $\boldsymbol{\tau}_s^*$  from the Newtonian solvent, and  $\mathbf{S}^*$  from the polymer solute:

$$\boldsymbol{\tau}^* = \boldsymbol{\tau}_s^* + \mathbf{S}^*, \quad (2.3)$$

$$\boldsymbol{\tau}_s^* = \eta_s^*(\nabla \mathbf{u}^* + (\nabla \mathbf{u}^*)^T), \quad (2.4)$$

$$\mathbf{S}^* + \lambda \mathbf{S}_{(1)}^* = \eta_p^*(\mathbf{D}^* - \mu \lambda (\mathbf{D}^* \cdot \mathbf{D}^*) + \frac{1}{2} \mu \lambda (\mathbf{D}^* : \mathbf{D}^*) \mathbf{I}), \quad (2.5)$$

where  $\mathbf{D}^*$  is the strain rate tensor  $\nabla \mathbf{u}^* + (\nabla \mathbf{u}^*)^T$ ,  $\mathbf{I}$  the unit tensor,  $\lambda$  the fluid relaxation time,  $\mu$  a dimensionless parameter, and  $\eta_s^*$ ,  $\eta_p^*$  the viscosity contributions from the solvent and polymers, respectively. The subscript (1) stands here for the upper-convected derivative defined by

$$\mathbf{S}_{(1)}^* = (\mathbf{u}^* \cdot \nabla) \mathbf{S}^* - \mathbf{S}^* \cdot \nabla \mathbf{u}^* - (\nabla \mathbf{u}^*)^T \cdot \mathbf{S}^*. \quad (2.6)$$

We scale the velocity with the mean velocity,  $U_m^0$ , in a straight pipe with the same radius and under the same pressure gradient as the curved pipe, the characteristic length is the pipe radius,  $a$ , and the extra stress and pressure are scaled with  $\eta^* U_m^0/a$  where  $\eta^* = \eta_s^* + \eta_p^*$ . The non-dimensional forms of the governing equations thus become

$$R_n(\mathbf{u} \cdot \nabla) \mathbf{u} = -\nabla P + \nabla \cdot (\boldsymbol{\tau}_s + \mathbf{S}), \quad (2.7)$$

$$\nabla \cdot \mathbf{u} = 0, \quad (2.8)$$

$$\boldsymbol{\tau}_s = \eta_s(\nabla \mathbf{u} + (\nabla \mathbf{u})^T), \quad (2.9)$$

$$\mathbf{S} + D_e \mathbf{S}_{(1)} = \eta_p(\mathbf{D} - \mu D_e (\mathbf{D} \cdot \mathbf{D}) + \frac{1}{2} \mu D_e (\mathbf{D} : \mathbf{D}) \mathbf{I}), \quad (2.10)$$

with the Reynolds number and Deborah number defined, respectively, by

$$R_n = \frac{\rho U_m^0 a}{\eta^*} \quad (2.11)$$

and

$$D_e = \frac{\lambda U_m^0}{a}. \quad (2.12)$$

This constitutive model predicts constant shear viscosity, and constant first and second normal-stress difference coefficients. Note that, if  $\mu = 0$  the model reduces to Oldroyd-B fluid, if  $\eta_p = 1$  it further reduces to UCM fluid, and  $D_e = 0$  or  $\eta_p = 0$  corresponds to the Newtonian case.

There are several definitions of the Dean number employed in the literature. A natural choice is based on the mean axial velocity,  $U_m$ , in the curved pipe, but it depends on the velocity field to be solved. Later theoretical and numerical investigators preferred to use the following Dean number:

$$D_n = 8 \left( \frac{2a}{R} \right)^{1/2} R_n. \quad (2.13)$$

Perturbation solutions provide valuable tests for numerical simulations; on the other hand, numerical simulations can examine the range of applicability of perturbation solutions. In the literature, there are numerous perturbation solutions for Newtonian

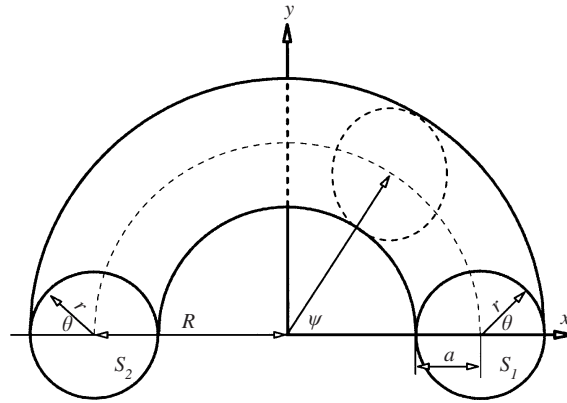


FIGURE 1. Sketch of the toroidal coordinate system.

laminar flow in curved pipes with small curvature ratio,  $\delta = a/R$ . Topakoglu (1967) obtained a perturbation solution for small Reynolds numbers without invoking the approximation of  $1/(R + r \cos \theta)$  being replaced by  $1/R$  in the Navier–Stokes equations. Bowen *et al.* (1991) presented an analytic perturbation solution for the creeping flow of UCM fluid in curved pipes. Robertson & Muller (1996) derived a perturbation solution for Oldroyd-B fluid that includes UCM fluid as a special case and contains the inertial effect. There is little difference between Topakoglu's and Robertson & Muller's predictions for Newtonian flows, and Bowen *et al.*'s and Robertson & Muller's predictions are almost identical for creeping UCM flow. Let us denote the volume flux in a curved pipe  $J_c$ , and that in a straight pipe of the same radius and under the same pressure gradient by  $J_s$ , then to the second order in  $\delta$ , in terms of our definitions of the Reynolds and Deborah numbers, the solution of Robertson & Muller (1996) is

$$\begin{aligned} \left(\frac{J_c}{J_s}\right)_R = & 1 + \frac{\delta^2}{48} \left\{ 1 - 4R_n^2 \left( \frac{11}{360} + 4R_n^2 \frac{1541}{87\,091\,200} \right) \right. \\ & + 4D_e^2 (\eta_p^2) \frac{8}{3} \left( 1 - \frac{4}{15} D_e^2 \eta_p (3 - 2\eta_p) \right) \\ & + 4D_e R_n \eta_p \frac{1}{26\,880} (4R_n^2 + 5376) \\ & \left. - 16D_e^2 R_n^2 \eta_p \frac{1}{60\,480} (792 - 691\eta_p) - 16D_e^3 R_n \eta_p^2 \frac{1}{90} (15 - 11\eta_p) \right\}. \quad (2.14) \end{aligned}$$

They also gave analytic solutions for the stream function of the secondary flow, to which we compare our numerical solutions. The expression for the stream function up to  $O(\delta^2)$  is very lengthy, and the reader is referred to the original paper. The flow resistance (the friction factor or the drag) is generally expressed in terms of the ratio of the pressure gradient in a curved pipe,  $f_c$ , to the pressure gradient in a straight pipe,  $f_s$ , carrying the same volume flux, thus

$$\frac{f_c}{f_s} = \left(\frac{J_c}{J_s}\right)^{-1}. \quad (2.15)$$

### 3. Three criteria of momentum and torque balances

Let us consider the flow in a curved pipe in terms of the toroidal coordinate system illustrated by figure 1. Since the flow is fully developed,

$$\frac{\partial}{\partial \psi} = 0 \quad \text{for all the variables except } \frac{\partial P}{\partial \psi} = C, \quad (3.1)$$

where  $C$  is a given constant. We can split the pressure as  $P = p(r, \theta) + f(\psi)$  and, without loss of generality, further simplify it as

$$P = p(r, \theta) + C\psi, \quad (3.2)$$

thus the total stress  $\Sigma$  can be expressed by

$$\Sigma = \sigma - C\psi I = \tau(r, \theta) - p(r, \theta)I - C\psi I, \quad (3.3)$$

where  $I$  is the unit tensor. The following analyses are carried out for the control volume that consists of the pipe wall and two cross-sections,  $\psi = 0$  and  $\psi = \pi$ , named  $S_1$  and  $S_2$ , respectively.

#### 3.1. Torque balance

The torque with respect to the curvature centre of the pipe exerted by the pipe wall on the fluid is

$$T_1 = \int_{\psi=0}^{\pi} \int_{\theta=0}^{2\pi} \sigma_{r\psi} (R + a \cos \theta)^2 a d\theta d\psi = \pi \int_{\theta=0}^{2\pi} \sigma_{r\psi} (R + a \cos \theta)^2 a d\theta. \quad (3.4)$$

The torque produced by the stresses on the two cross-sections  $S_1$  and  $S_2$  cancel each other except for the pressure  $C\psi$  which is

$$T_2 = \int_{r=0}^a \int_{\theta=0}^{2\pi} \pi C (R + r \cos \theta) r d\theta dr = \pi^2 a^2 RC. \quad (3.5)$$

The torque-balance principle requires  $T_1 = T_2$ , that is

$$\int_{\theta=0}^{2\pi} \sigma_{r\psi} (R + a \cos \theta)^2 a d\theta = \pi a^2 RC. \quad (3.6)$$

In general, the difference in the torques enables us to define an error index,  $E_t$ , to assess the numerical solutions,

$$ER_t = (T_1 - T_2)/T_2. \quad (3.7)$$

#### 3.2. Momentum balance in the x-direction

The force exerted by the wall stresses that have a contribution in the x-direction is

$$F_{x1} = - \int_{\psi=0}^{\pi} \int_{\theta=0}^{2\pi} \sigma_{r\psi} \sin \psi (R + a \cos \theta) a d\theta d\psi = -2 \int_{\theta=0}^{2\pi} \sigma_{r\psi} (R + a \cos \theta) a d\theta. \quad (3.8)$$

The force produced by the wall pressure is

$$F_{x2} = \int_{\psi=0}^{\pi} \int_{\theta=0}^{2\pi} [-p(r, \theta) - C\psi] \cos \theta \cos \psi (R + a \cos \theta) a d\theta d\psi = 2\pi a^2 C. \quad (3.9)$$

The force on the two cross-sections  $S_1$  and  $S_2$  is

$$F_{x3} = -2 \int_{r=0}^a \int_{\theta=0}^{2\pi} (\sigma_{r\psi} \cos \theta - \sigma_{\theta\psi} \sin \theta) r d\theta dr. \quad (3.10)$$

The change of the momentum flux in the  $x$ -direction is

$$Q_x = 2 \int_{r=0}^a \int_{\theta=0}^{2\pi} \rho u_x u_\psi r d\theta dr. \quad (3.11)$$

Thus the momentum-balance principle requires

$$F_{x1} + F_{x2} + F_{x3} + Q_x = 0, \quad (3.12)$$

and therefore a measure of the numerical error may be defined as

$$ER_x = (F_{x1} + F_{x2} + F_{x3} + Q_x) / (F_{x2} + F_{x3} + Q_x). \quad (3.13)$$

### 3.3. Momentum balance in the $y$ -direction

The force exerted by the wall stresses that have a contribution in the  $y$ -direction is

$$\begin{aligned} F_{y1} &= \int_{\psi=0}^{\pi} \int_{\theta=0}^{2\pi} (\sigma_{rr} \cos \theta - \sigma_{r\theta} \sin \theta) \sin \psi (R + a \cos \theta) a d\theta d\psi \\ &= 2 \int_{\theta=0}^{2\pi} (\sigma_{rr} \cos \theta - \sigma_{r\theta} \sin \theta) (R + a \cos \theta) a d\theta. \end{aligned} \quad (3.14)$$

The wall pressure  $C\psi$  is balanced by the pressure on the cross-sections  $S_1$  and  $S_2$ :

$$\int_{\psi=0}^{\pi} \int_{\theta=0}^{2\pi} C\psi \cos \theta \sin \psi (R + a \cos \theta) a d\theta d\psi = \pi a^2 C\pi. \quad (3.15)$$

On the cross-sections  $S_1$  and  $S_2$  the fluid stress produces

$$F_{y2} = -2 \int_{r=0}^a \int_{\theta=0}^{2\pi} \sigma_{\psi\psi} r d\theta dr. \quad (3.16)$$

The change of the momentum flux in the  $y$ -direction is

$$Q_y = 2 \int_{r=0}^a \int_{\theta=0}^{2\pi} \rho u_\psi^2 r d\theta dr. \quad (3.17)$$

The momentum-balance in the  $y$ -direction requires

$$F_{y1} + F_{y2} + Q_y = 0, \quad (3.18)$$

thus a measure of the numerical solutions may be defined as

$$ER_y = (F_{y1} + F_{y2} + Q_y) / (F_{y2} + Q_y). \quad (3.19)$$

## 4. Numerical methods

The dimensionless solution of Poiseuille flow in a straight circular pipe is

$$u_s = -\frac{1}{4} \frac{dP}{ds} (1 - r^2), \quad (4.1)$$

where  $s$  is the axial distance,  $r$  the radial position. Note that this solution holds for both Newtonian and Oldroyd-3-constant fluids. Hence the mean velocity is

$$U_m^0 = -\frac{1}{8} \frac{dP}{ds}. \quad (4.2)$$



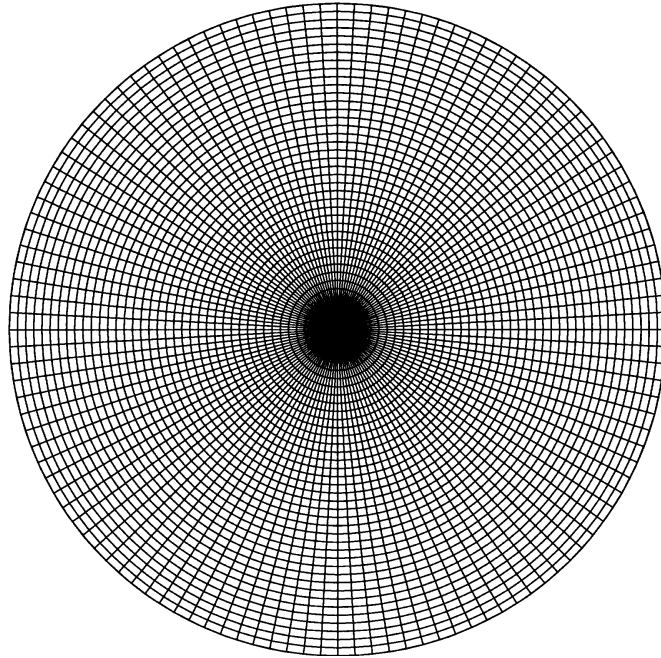


FIGURE 2. The finite element mesh used in the present computations.

Since  $U_m^0$  is the scaling velocity, it follows from equation (3.2) that

$$\frac{1}{R} \frac{\partial P}{\partial \psi} = \frac{C}{R} = -8. \quad (4.3)$$

The fully developed flow assumption makes the problem two-dimensional; the computational domain consists of cross-sections with varying thickness according to the bending curvature. For the curved pipe geometry, the toroidal coordinate system illustrated by figure 1 is commonly preferred because of its orthogonality and ability to fit the pipe wall with a coordinate line. The transformation from the rectangular coordinates  $(x, y, z)$  to the toroidal coordinate system  $(r, \theta, \psi)$  is

$$x = (R + r \cos \theta) \cos \psi, \quad y = (R + r \cos \theta) \sin \psi, \quad z = r \sin \theta. \quad (4.4)$$

The finite element mesh used in this study is shown in figure 2, where, due to a limitation of the graphics tool used, each element is plotted as four sub-elements. Because the flow is symmetric about the planes  $\theta = 0$  and  $\theta = \pi$ , only a half-domain in figure 2 is taken as the computational domain and the results obtained are plotted on the whole domain according to the symmetry rule.

The numerical simulation of viscoelastic flows still remains a challenging task in terms of accuracy, stability, convergence and demand for computer resources. We use the  $h$ - $p$  type finite element method to obtain high accuracy and efficiency. A set of hierarchic basis functions proposed by Szabo & Babuska (1991) is adopted for the finite element spaces. In our  $h$ - $p$  extension, the velocity and stress variables are interpolated with the same order of polynomials while the pressure is kept one order lower than the velocity variables. Hence, given a finite element mesh, a discretization is specified by its interpolation order of the velocity variables. In the following, we

label a discretization by  $PO$  followed by its highest velocity interpolation order in the computational domain, e.g.  $PO2, PO3, PO4$ , etc.

A common practice in the finite element computations for viscoelastic flows is to use the Galerkin weighted residual method for the momentum and continuity equations, and the streamline upwind Petrov–Galerkin (SUPG) technique of Brooks & Hughes (1982) for the constitutive equation; the latter is due to the hyperbolic character in the streamline direction with respect to the stress variables. In this study the recently developed Galerkin/least-square method proposed by Hughes, Franca & Hubert (1989) is employed to further stabilize the algorithm. It adds some residual functions of the Euler–Lagrangian equations to the usual Galerkin formulation to enhance its stability without damaging its accuracy. In the field of viscoelastic flows, the Galerkin/least-square methods include the discrete elastic-viscous-split-stress (DEVSS) method proposed by Guénette & Fortin (1995) and the MIX1 method proposed by the present authors. Unlike DEVSS, the MIX1 method need not solve for the strain-rate variable; it is thus considerably less costly but has the same level of accuracy and stability as the DEVSS method; the readers are referred to Fan, Tanner & Phan-Thien (1999) for the details.

Let  $\Omega$  be the flow domain and  $\partial\Omega$  its boundary. On  $\partial\Omega$ , the partial boundaries  $\partial\Omega_u$ ,  $\partial\Omega_N$  are identified with boundary conditions for the velocity  $\mathbf{u}$  and the traction force  $\mathbf{t}$ , respectively. The variational formulation, named MIX1, used for the steady flow of Oldroyd-3-constant fluids can be stated as follows:

Find the set  $(\mathbf{S}, \mathbf{u}, p) \in \mathcal{T} \times \mathcal{V} \times \mathcal{P}$  such that,  $\forall \Phi_u \in \mathcal{V}$ ,  $\forall \Phi_p \in \mathcal{P}$ ,  $\forall \Phi_s \in \mathcal{T}$ ,

$$\int_{\Omega} R_n((\mathbf{u} \cdot \nabla)\mathbf{u}) \cdot \Phi_u d\Omega + \int_{\Omega} (\eta_s(\nabla\mathbf{u} + \nabla\mathbf{u}^T) + \mathbf{S}) : \nabla\Phi_u - P\nabla \cdot \Phi_u d\Omega + \int_{\Omega} \alpha_c(\nabla \cdot \mathbf{u})(\nabla \cdot \Phi_u) d\Omega = \int_{\partial\Omega_N} \mathbf{t} \cdot \Phi_u d\partial\Omega, \quad (4.5)$$

$$\int_{\Omega} (\nabla \cdot \mathbf{u})\Phi_p d\Omega = 0, \quad (4.6)$$

$$\int_{\Omega} (\mathbf{S} + D_e\mathbf{S}_{(1)} - \eta_p(\mathbf{D} - \mu D_e(\mathbf{D} \cdot \mathbf{D}) + \frac{1}{2}\mu D_e(\mathbf{D} : \mathbf{D})\mathbf{I})) : (\Phi_s + k\mathbf{u} \cdot \nabla\Phi_s) d\Omega = 0, \quad (4.7)$$

where  $\mathbf{D} = \nabla\mathbf{u} + \nabla\mathbf{u}^T$ ,  $\mathcal{T}$ ,  $\mathcal{V}$ ,  $\mathcal{P}$  denote the function spaces defined on  $\Omega$  and spanned by the basis functions  $\Phi_s$ ,  $\Phi_u$ ,  $\Phi_p$ , for the extra stress, velocity and pressure, respectively. In the toroidal coordinate system  $d\Omega = (R + r \cos \theta)r d\theta dr$ .

In equation (4.5) the term containing  $\alpha_c$  is a least-square residual of the continuity equation, and if  $\alpha_c$  is viewed as a kind of bulk viscosity – one may take  $\alpha_c = 1$ . Our previous study (Fan *et al.* 1999) showed that constant  $\alpha_c$  has a satisfactory performance for stabilization and is robust within a relatively large range of values. In the present problem, the continuity equation contains only the velocity components of the secondary flow and they are at least two orders of magnitude smaller than the axial velocity component. To effect the stabilization, we tried some large values of  $\alpha_c$ , say  $\alpha_c = 100$ , and found that not only does a large  $\alpha_c$  not harm the accuracy of the momentum balance (the only possible side-effect), but it reduces errors of mass conservation. Equation (4.7) is the SUPG formulation for the constitutive equation in which we choose the parameter  $k = h/u_m$ , where  $h$  is the element size along the local flow direction and  $u_m$  is a mean value of the velocity magnitude over the element. This choice comes from the investigation of Fan & Crochet (1995); it guarantees that the upwind term approaches zero together with the velocity on stationary walls.

For the present problem, the no-slip condition of the velocity is applied on the pipe wall; the normal velocity component  $u_\theta$  and the boundary traction  $\mathbf{t}$  are set to zero on the symmetric plane. No essential stress boundary condition is needed for the viscoelastic flows.

After discretization, the nonlinear set of equations for the unknown variables  $(\mathbf{u}, p)$  or  $(\mathbf{S}, \mathbf{u}, p)$  is solved by the Newton iteration scheme. Convergence of the iteration for the Newtonian flows is very easy to achieve because the secondary flow is rather weak compared to the main axial flow; even at high Reynolds numbers with large curvature ratios we did not need to invoke any stabilization technique. The calculations for the viscoelastic flows are much more difficult; augmentation of the elasticity level must be carried out carefully, in which the Deborah number  $D_e$  was increased from zero (Newtonian flow) to a designated value. Generally, after five iterations the maximum variation  $\max\{\delta\mathbf{S}, \delta\mathbf{u}, \delta p\}$  is less than  $10^{-4}$ , indicating a quadratic convergence behaviour.

An important measurement of the secondary flow is the stream function in the cross-section. To satisfy the continuity equation (2.8), the stream function,  $F$ , in the toroidal coordinate system can be defined as

$$u_r = -\frac{1}{1 + \delta \cos \theta} \frac{\partial F}{r \partial \theta}, \quad u_\theta = \frac{1}{1 + \delta \cos \theta} \frac{\partial F}{\partial r}; \quad (4.8)$$

then the corresponding Poisson equation

$$\nabla \cdot \nabla F = (1 + r \cos \theta) \left( \frac{\partial u_\theta}{\partial r} - \frac{\partial u_r}{r \partial \theta} + \frac{u_\theta}{r} \right) + \frac{2(u_\theta \cos \theta + u_r \sin \theta)}{R} \quad (4.9)$$

can be solved by using the ordinary finite element method. The boundary condition is  $F = 0$  on the pipe wall, as well as on the symmetry plane.

Let us define two maximum stream functions  $F_{\max}$  and  $F_{\max}^*$  as follows:

$$F_{\max} = \max_{i=1}^N |F_i|, \quad (4.10)$$

$$F_{\max}^* = F_{\max} \left( \frac{J_s}{J_c} \right), \quad (4.11)$$

where  $F_i$  is the node value of the stream function from our finite element computation and  $N$  is the total number of mesh nodes;  $J_s$  and  $J_c$  are the axial volume flux through the straight and curved pipes, respectively, under the same pressure gradient. Note that in our computation, the pressure gradient is a fixed constant (equation (4.3)) and the boundary value of  $F$  is zero, hence  $F_{\max}$  physically represents the volumetric flux of the secondary flow per unit work consumption and  $F_{\max}^*$  can represent the volumetric flux of the secondary flow per unit axial flux. These two parameters are used to quantify the intensity of the secondary flow in this study. Furthermore, we define a relative root-mean-square (r.m.s) deviation of the stream function of our computation from that of Robertson & Muller's perturbation solution as

$$F_{rms} = \frac{1}{F_{\max}} \sqrt{\frac{1}{N} \sum_1^N (F_i - F_{Robertson})^2}. \quad (4.12)$$

| $\delta$ | $R_n$  | $D_n$ | $f_c/f_s$ | $ER_t$               | $ER_x$               | $ER_y$               |
|----------|--------|-------|-----------|----------------------|----------------------|----------------------|
| 0.5      | 12.0   | 96    | 1.0761    | $8.4 \times 10^{-5}$ | $2.0 \times 10^{-4}$ | $5.1 \times 10^{-5}$ |
| 0.5      | 125.0  | 1000  | 1.6912    | $8.2 \times 10^{-4}$ | $5.5 \times 10^{-4}$ | $3.3 \times 10^{-4}$ |
| 0.5      | 375.0  | 3000  | 2.2590    | $3.5 \times 10^{-3}$ | $2.9 \times 10^{-3}$ | $8.1 \times 10^{-4}$ |
| 0.5      | 625.0  | 5000  | 2.5985    | $6.1 \times 10^{-3}$ | $5.2 \times 10^{-3}$ | $1.1 \times 10^{-3}$ |
| 0.5      | 1250.0 | 10000 | 3.1497    | $1.2 \times 10^{-2}$ | $1.1 \times 10^{-2}$ | $1.7 \times 10^{-3}$ |
| 0.5      | 2000.0 | 16000 | 3.6111    | $1.9 \times 10^{-2}$ | $1.8 \times 10^{-2}$ | $2.3 \times 10^{-3}$ |
| 0.5      | 3000.0 | 24000 | 4.0697    | $2.9 \times 10^{-2}$ | $2.8 \times 10^{-2}$ | $2.9 \times 10^{-3}$ |

TABLE 1. Finite element solutions using *PO2* for the curvature ratio 0.5.

| $\delta$ | $R_n$   | <i>PO</i>  | $f_c/f_s$ | $F_{\max}$ | $ER_t$               | $ER_x$               | $ER_y$               |
|----------|---------|------------|-----------|------------|----------------------|----------------------|----------------------|
| 0.01     | 8838.83 | <i>PO2</i> | 2.8836    | 0.002934   | $1.8 \times 10^{-2}$ | $1.8 \times 10^{-2}$ | $2.2 \times 10^{-3}$ |
| 0.01     | 8838.83 | <i>PO3</i> | 2.8858    | 0.002929   | $3.3 \times 10^{-3}$ | $3.3 \times 10^{-3}$ | $5.2 \times 10^{-4}$ |
| 0.01     | 8838.83 | <i>PO4</i> | 2.8858    | 0.002929   | $6.3 \times 10^{-4}$ | $6.3 \times 10^{-4}$ | $3.8 \times 10^{-5}$ |
| 0.01     | 8838.83 | <i>PO5</i> | 2.8858    | 0.002929   | $3.2 \times 10^{-5}$ | $3.2 \times 10^{-5}$ | $9.2 \times 10^{-7}$ |
| 0.2      | 1976.42 | <i>PO2</i> | 3.0032    | 0.011717   | $1.5 \times 10^{-2}$ | $1.4 \times 10^{-2}$ | $1.9 \times 10^{-3}$ |
| 0.2      | 1976.42 | <i>PO3</i> | 3.0052    | 0.011697   | $2.9 \times 10^{-3}$ | $2.8 \times 10^{-3}$ | $4.4 \times 10^{-4}$ |
| 0.2      | 1976.42 | <i>PO4</i> | 3.0052    | 0.011697   | $4.5 \times 10^{-4}$ | $4.2 \times 10^{-4}$ | $3.4 \times 10^{-5}$ |
| 0.2      | 1976.42 | <i>PO5</i> | 3.0052    | 0.011697   | $2.1 \times 10^{-5}$ | $2.2 \times 10^{-5}$ | $3.2 \times 10^{-7}$ |
| 0.5      | 2000.0  | <i>PO2</i> | 3.6111    | 0.013384   | $1.9 \times 10^{-2}$ | $1.8 \times 10^{-2}$ | $2.3 \times 10^{-3}$ |
| 0.5      | 2000.0  | <i>PO3</i> | 3.6182    | 0.013366   | $3.4 \times 10^{-3}$ | $3.1 \times 10^{-3}$ | $4.7 \times 10^{-4}$ |
| 0.5      | 2000.0  | <i>PO4</i> | 3.6183    | 0.013366   | $6.6 \times 10^{-4}$ | $5.8 \times 10^{-4}$ | $5.4 \times 10^{-5}$ |
| 0.5      | 2000.0  | <i>PO5</i> | 3.6183    | 0.013366   | $1.5 \times 10^{-5}$ | $1.9 \times 10^{-5}$ | $3.2 \times 10^{-6}$ |

TABLE 2. Results of the *h-p* extension computation for the Newtonian fluid.

## 5. Inertial flow of Newtonian fluids

We have calculated the cases with curvature ratio  $\delta = 0.001, 0.01, 0.2, 0.5$ . Very satisfactory agreement between our finite element solutions and Robertson's perturbation solutions was observed for low Reynolds numbers with  $\delta = 0.001, 0.01$ : the agreement on the flow resistance reached within a tolerance of  $10^{-6}$  while the agreement on the stream function is within  $10^{-4}$ . However, the upper limit of the Reynolds number for the perturbation solution to be valid decreases rapidly as the curvature ratio increases. We also compared our predictions with that of Yanase *et al.* (1989) who use the Fourier–Chebyshev spectral method and assume the curvature can be neglected in the governing equations except for the centrifugal term; our solutions for the case of  $\delta = 0.001$  agreed well with their predictions. Soh & Berger (1987) studied the curvature effect by solving the full Navier–Stokes equation using a finite difference method; for the case of  $\delta = 0.01$ , the agreement on the flow resistance between their predictions and ours is within  $10^{-2}$ . For the large curvature ratio,  $\delta = 0.2$ , the available reference data is from Soh & Berger (1987) and Austin & Seader (1973), where the latter also used a finite difference method; comparisons showed that our predictions agreed better with Soh & Berger's than with Austin & Seader's. For the largest curvature ratio,  $\delta = 0.5$ , for which there are no available data in the literature, we list our predictions in table 1.

Generally, as the Reynolds number increases, the solution's accuracy will deteriorate; this is due to the formation of boundary layers near the pipe wall. To examine

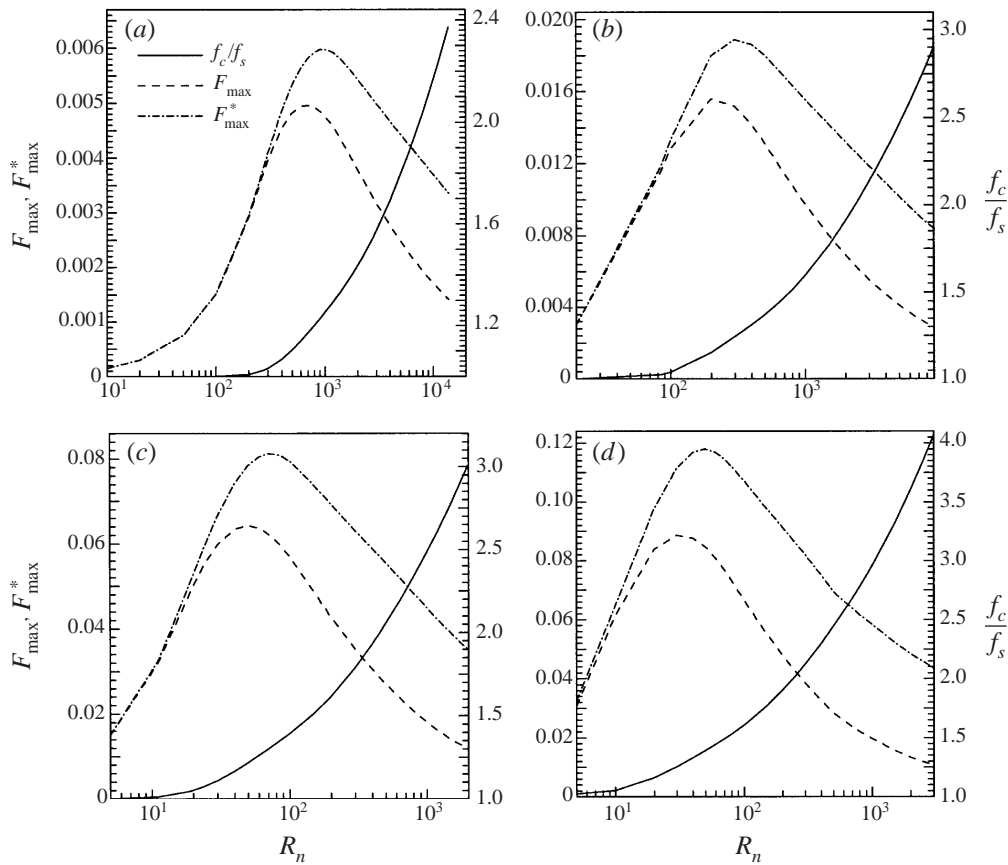


FIGURE 3. The flow resistance  $f_c/f_s$  and secondary volume fluxes  $F_{\max}, F_{\max}^*$  versus the Reynolds number  $R_n$ ; Newtonian fluid. (a)  $\delta = 0.001$ , (b) 0.01, (c) 0.2, (d) 0.5.

the accuracy of our solutions, we carried out successive  $h$ - $p$  extension computations in which eight layers of the elements near the wall were enriched to order-3 ( $PO3$ ), then four layers of the elements near the wall were increased to order-4 ( $PO4$ ) and finally, two layers of the elements near the wall were increased to order-5 ( $PO5$ ). In table 2, the three error indicators  $ER_t$ ,  $ER_x$  and  $ER_y$  show the excellent convergent property of our  $h$ - $p$  computations for the cases of  $\delta = 0.01, 0.2, 0.5$  with high Reynolds numbers.

Figure 3 shows the variations of the flow resistance and the maximum stream functions with the Reynolds number. For all the curvature ratios considered, the flow resistance is a monotonically increasing function of the Reynolds number. The stream functions  $F_{\max}$  and  $F_{\max}^*$ , however, increase to a peak value at a certain Reynolds number after which they decrease. As far as we are aware, this behaviour of the stream function has not been explicitly reported in the literature and we believe its significance is important because here  $F_{\max}$  represents the volumetric flux of the secondary flow per unit work consumption and  $F_{\max}^*$  the volumetric flux of the secondary flow per unit axial volumetric flux.

The boundary layer theory developed by Ito (1969) and Mashelkar & Devarajan (1976) assumes that in the core region of the pipe, the centrifugal force is balanced

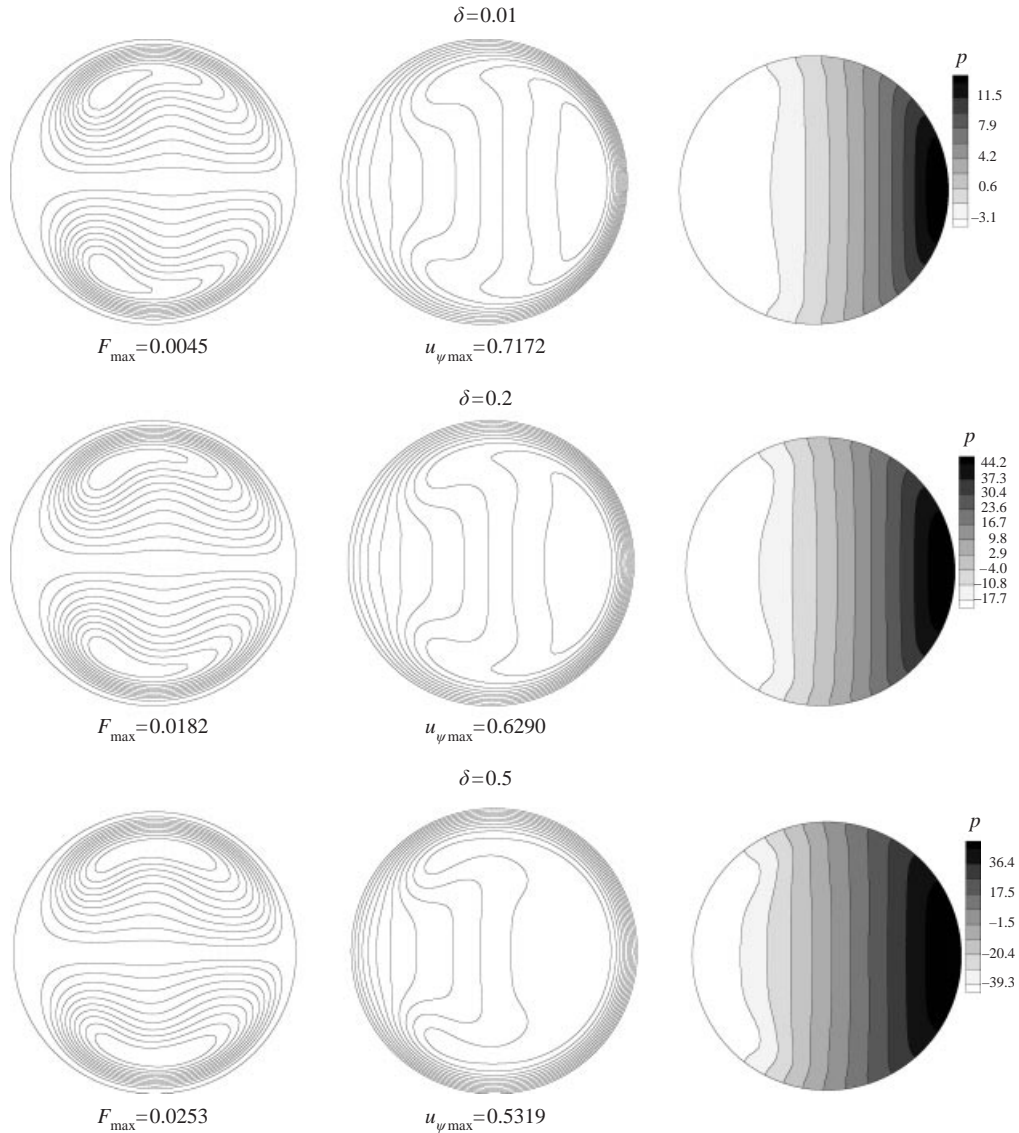


FIGURE 4. Contours of the stream function  $F$ , the axial velocity  $u_\psi$  and the pressure  $p$  of Newtonian fluid with the Dean number  $D_n = 5000$ . The contour levels are equally divided between the maximum and minimum values. The left is the inner bend side, the right is the outer bend side. The secondary flow is counter-clockwise in the upper half of the cross-section and clockwise in the lower half.

by the pressure gradient solely (see also the Appendix), i.e.

$$R_n \frac{u_\psi^2}{Q} \approx \frac{\partial p}{\partial x}, \tag{5.1}$$

where  $Q = R + \cos \theta$ . This leads to

$$p \approx p(x), \quad u_\psi \approx u_\psi(x), \tag{5.2}$$

where  $x$  is the bending direction defined in figure 1. Thus in the wall region where  $u_\psi \ll 1$ , we can identify the pressure gradient as the driving force for the secondary flow.

In figure 4 we plot the streamlines of the secondary flow, the contours of the axial

| $\delta$ | $D_e$ | $f_c/f_s$ | $(f_c/f_s)_R$ | $F_{rms}$            | $ER_t$               | $ER_x$               | $ER_y$               |
|----------|-------|-----------|---------------|----------------------|----------------------|----------------------|----------------------|
| 0.001    | 5.0   | 1.000031  | 1.000031      | $3.3 \times 10^{-4}$ | $4.4 \times 10^{-6}$ | $4.4 \times 10^{-6}$ | $1.8 \times 10^{-3}$ |
| 0.001    | 10.0  | 1.000566  | 1.000571      | $5.1 \times 10^{-3}$ | $1.1 \times 10^{-5}$ | $1.1 \times 10^{-5}$ | $1.7 \times 10^{-3}$ |
| 0.001    | 20.0  | 1.008113  | 1.009482      | $7.1 \times 10^{-2}$ | $7.4 \times 10^{-6}$ | $7.3 \times 10^{-6}$ | $1.8 \times 10^{-3}$ |
| 0.001    | 30.0  | 1.027562  | 1.050200      | $2.6 \times 10^{-1}$ | $3.9 \times 10^{-6}$ | $3.6 \times 10^{-6}$ | $2.3 \times 10^{-3}$ |
| 0.01     | 1.0   | 0.999982  | 0.999982      | $4.3 \times 10^{-5}$ | $7.9 \times 10^{-7}$ | $7.8 \times 10^{-7}$ | $1.0 \times 10^{-3}$ |
| 0.01     | 4.0   | 1.001139  | 1.001161      | $1.2 \times 10^{-2}$ | $1.3 \times 10^{-5}$ | $1.2 \times 10^{-5}$ | $1.7 \times 10^{-3}$ |
| 0.01     | 6.0   | 1.006136  | 1.006926      | $5.8 \times 10^{-2}$ | $9.7 \times 10^{-6}$ | $8.2 \times 10^{-6}$ | $1.7 \times 10^{-3}$ |
| 0.01     | 10.0  | 1.030431  | 1.060485      | $3.0 \times 10^{-1}$ | $8.4 \times 10^{-6}$ | $5.3 \times 10^{-6}$ | $2.4 \times 10^{-3}$ |
| 0.2      | 0.2   | 0.998836  | 0.998816      | $9.0 \times 10^{-3}$ | $5.3 \times 10^{-6}$ | $1.3 \times 10^{-5}$ | $2.1 \times 10^{-3}$ |
| 0.2      | 0.6   | 0.996331  | 0.996288      | $7.5 \times 10^{-3}$ | $1.6 \times 10^{-6}$ | $8.6 \times 10^{-6}$ | $2.0 \times 10^{-3}$ |
| 0.2      | 1.0   | 0.993204  | 0.992702      | $1.6 \times 10^{-2}$ | $1.4 \times 10^{-5}$ | $5.6 \times 10^{-6}$ | $1.8 \times 10^{-3}$ |
| 0.2      | 2.0   | 1.002926  | 1.001539      | $1.6 \times 10^{-1}$ | $2.3 \times 10^{-5}$ | $4.2 \times 10^{-5}$ | $1.8 \times 10^{-3}$ |
| 0.2      | 2.5   | 1.018081  | 1.037564      | $3.3 \times 10^{-1}$ | $4.7 \times 10^{-5}$ | $4.9 \times 10^{-5}$ | $2.1 \times 10^{-3}$ |
| 0.5      | 0.4   | 0.987482  | 0.986468      | $6.3 \times 10^{-2}$ | $4.1 \times 10^{-5}$ | $9.7 \times 10^{-5}$ | $3.6 \times 10^{-3}$ |
| 0.5      | 1.0   | 0.968315  | 0.956069      | $7.5 \times 10^{-2}$ | $2.3 \times 10^{-5}$ | $1.2 \times 10^{-4}$ | $2.7 \times 10^{-3}$ |
| 0.5      | 2.0   | 1.008786  | 1.009700      | $4.8 \times 10^{-1}$ | $7.9 \times 10^{-5}$ | $4.2 \times 10^{-4}$ | $2.4 \times 10^{-3}$ |
| 0.5      | 2.2   | 1.022363  | 1.078689      | $6.5 \times 10^{-1}$ | $1.5 \times 10^{-4}$ | $4.6 \times 10^{-4}$ | $2.5 \times 10^{-3}$ |

TABLE 3. Comparison of the solutions using  $PO2$  with the perturbation solutions of Robertson & Muller (1996); the creeping flow of the UCM fluid.  $F_{rms}$  is defined in (4.12).

velocity  $u_p$ , and pressure. The picture qualitatively agrees with the previous literature (see, e.g., Daskopoulos & Lenhoff 1989, Austin & Seader 1973). It can be observed that for the fixed Dean number  $D_n = 5000$ , the curvature effect is to reduce the axial flow and enhance the secondary flow. The region on which  $u_p \approx u_p(x)$  shrinks as the curvature ratio increases, and also the approximation  $p \approx p(x)$  holds on the outer part of the core region where  $u_p$  has larger values.

### 6. Creeping flow of UCM fluid

Through the creeping flow of UCM fluid we can examine the sole effect of the first normal-stress difference, which is proportional to the Deborah number and to the square of the shear rate in a simple shear flow. Table 3 demonstrates the excellent agreement of our computation with the perturbation solution of Robertson & Muller (1996) for UCM fluid; also through table 3 one can estimate, in terms of the Deborah number, the range of validity of the perturbation solution.

For UCM fluid, as the Deborah number increases, stress boundary layers near the pipe wall are formed; this deteriorates the solution's accuracy. Similar computations of the  $h$ - $p$  extension to that for Newtonian fluid were carried out for UCM fluid. In table 4, the convergent property of  $ER_t$ ,  $ER_x$  and  $ER_y$  is not as perfect as in the Newtonian case. Table 5 lists the number of equations needed to be solved in these calculations. Figure 5 plots the stress components  $S_{\psi\psi}$  and  $S_{r\psi}$  on the pipe wall: as the interpolation order increases, the stress profiles show good convergent properties except near the stagnation point of the secondary flow, i.e. the outer bent point  $\theta = 0$ . It was also observed that with high Deborah numbers and low-order interpolations the 'Finger' tensor  $\mathbf{B} = \mathbf{S} + \mathbf{I}/D_e$  lost its positive definiteness at a few points on the

| $\delta$ | $D_e$ | $PO$  | $f_c/f_s$ | $F_{\max}$ | $ER_t$               | $ER_x$               | $ER_y$               |
|----------|-------|-------|-----------|------------|----------------------|----------------------|----------------------|
| 0.01     | 15.0  | $PO2$ | 1.069934  | 0.005774   | $1.2 \times 10^{-4}$ | $1.1 \times 10^{-4}$ | $3.7 \times 10^{-3}$ |
| 0.01     | 15.0  | $PO3$ | 1.069874  | 0.005773   | $1.3 \times 10^{-4}$ | $1.3 \times 10^{-4}$ | $2.1 \times 10^{-4}$ |
| 0.01     | 15.0  | $PO4$ | 1.069876  | 0.005773   | $8.4 \times 10^{-5}$ | $8.4 \times 10^{-5}$ | $2.6 \times 10^{-5}$ |
| 0.01     | 15.0  | $PO5$ | 1.069882  | 0.005773   | $6.7 \times 10^{-5}$ | $6.7 \times 10^{-5}$ | $2.8 \times 10^{-5}$ |
| 0.2      | 4.0   | $PO2$ | 1.073749  | 0.027088   | $3.2 \times 10^{-4}$ | $1.4 \times 10^{-4}$ | $3.0 \times 10^{-3}$ |
| 0.2      | 4.0   | $PO3$ | 1.073582  | 0.027079   | $1.6 \times 10^{-4}$ | $2.3 \times 10^{-4}$ | $1.6 \times 10^{-4}$ |
| 0.2      | 4.0   | $PO4$ | 1.073571  | 0.027078   | $1.2 \times 10^{-4}$ | $1.3 \times 10^{-4}$ | $3.8 \times 10^{-6}$ |
| 0.2      | 4.0   | $PO5$ | 1.073582  | 0.027079   | $8.8 \times 10^{-5}$ | $8.2 \times 10^{-5}$ | $3.2 \times 10^{-5}$ |

TABLE 4. Results of the  $h$ - $p$  extension computation for the creeping flow of the UCM fluid.

| Interpolation order | Number of unknowns |
|---------------------|--------------------|
| $PO2$               | 22896              |
| $PO3$               | 34690              |
| $PO4$               | 43092              |
| $PO5$               | 48598              |

TABLE 5. Number of unknowns to be solved for the  $h$ - $p$  extension computation.

wall near this stagnation point and this was rectified by higher-order interpolations. The convergence of the  $h$ - $p$  extension as a whole is satisfactory.

The analysis of the order of magnitude, given in the Appendix, concludes that in the core region where  $u_{\psi} \gg u_r, u_{\theta}$  the pressure gradient is balanced by the axial normal stress solely:

$$0 \approx \frac{\partial p}{\partial x} + \frac{S_{\psi\psi}}{Q}, \quad (6.1)$$

where  $Q = R + \cos \theta$ . Thus the secondary flow can be attributed to the momentum imbalance near the wall region where larger normal stress  $S_{\psi\psi}$  surpasses the pressure gradient, and the driving force turns out to be in the same direction as the Newtonian inertial flow. Figure 6 plots the streamlines of the secondary flow, the distributions of the axial velocity  $u_{\psi}$  and the pressure  $p$  for two relatively high Deborah numbers. Notice that  $p \approx p(x)$  holds in the core region and the pressure gradient is in the opposite direction to that of Newtonian inertial flow. Obviously, it is the relatively large axial normal stress near the wall that promotes a secondary flow in the same direction as the inertial secondary flow.

Figure 7 shows variations of the flow resistance and the maximum stream functions  $F_{\max}$  and  $F_{\max}^*$  with the Deborah number. The behaviours of the stream functions are similar to that for Newtonian fluid. They increase with the Deborah number to a maximum value then monotonically decrease. The flow resistance, however, first decreases to a minimum value then increases monotonically with the Deborah number. This kind of drag reduction phenomenon has been predicted by the perturbation solutions of Bowen *et al.* (1991) and Robertson & Muller (1996) for small curvature ratios; in figure 7, it is not detectable in the plot for the small curvature ratios  $\delta = 0.001, 0.1$  but is very apparent for the large curvature ratios  $\delta = 0.2, 0.5$ .

For each curvature ratio  $\delta$ , there is a limiting Deborah number  $D_{e,\max}$  above which our Newton iteration algorithm failed to converge. We carried out the  $h$ - $p$  extension calculations to exclude as much of numerical errors as possible, and it seems that



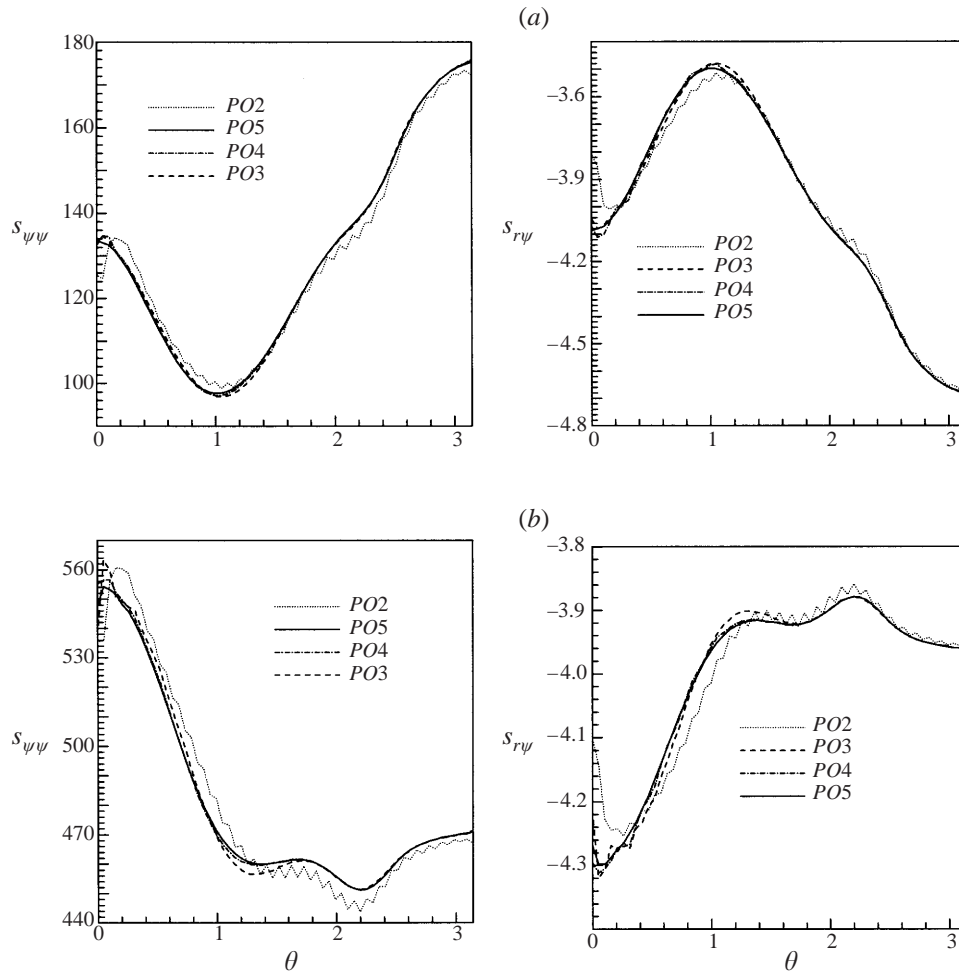


FIGURE 5. The stress profiles  $S_{\psi\psi}$ ,  $S_{r\psi}$  on the pipe wall for the UCM fluid under the  $h$ - $p$  extension calculations in creeping flow. (a)  $\delta = 0.2$ ,  $D_e = 4$ ; (b)  $\delta = 0.01$ ,  $D_e = 15$ .

the limiting Deborah number is due to the instability of the constitutive model. Table 6 shows that the dimensionless parameter  $\delta^{1/2}D_e$  can be used to characterize the convergence breakdown problem. It is the same as the parameter proposed by McKinley *et al.* (1996) for the onset of purely elastic instabilities. McKinley *et al.*'s criterion can be deduced from the nonlinear terms in the upper-convected derivative in the constitutive equations, and, we believe, it is these nonlinear terms that constitute the major difficulty for the steady computations.

Let us express the set of discretized finite element equations for an unsteady viscoelastic flow problem as

$$\mathbf{M} \frac{d\mathbf{a}}{dt} + \mathbf{R}(\mathbf{a}) = \mathbf{0}, \tag{6.2}$$

where  $\mathbf{a}$  is the unknown variable vector,  $\mathbf{M}$  is the mass matrix and the nonlinear vector  $\mathbf{R}(\mathbf{a})$  represents the spatial discretization of the problem and corresponds exactly to the equation set for the steady flow. Suppose we have a steady-state solution  $\mathbf{a}_s$  which

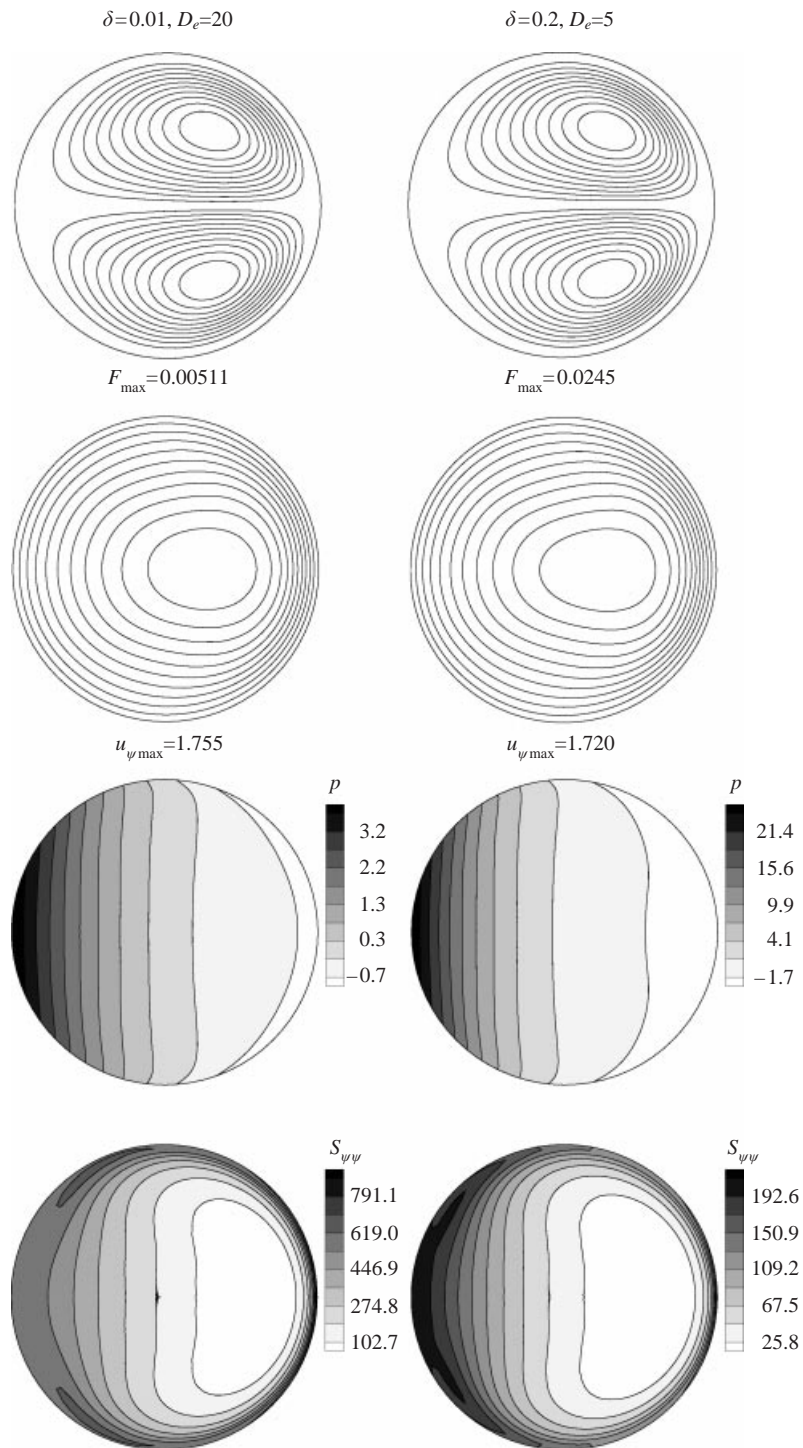


FIGURE 6. Contours of the stream function  $F$ , the axial velocity  $u_\psi$ , the pressure  $p$  and the axial normal stress  $S_{\psi\psi}$  for the creeping flow of UCM fluid. The contour levels are equally divided between the maximum and minimum values. The secondary flow is counter-clockwise in the upper half and clockwise in the lower half of the cross-section.

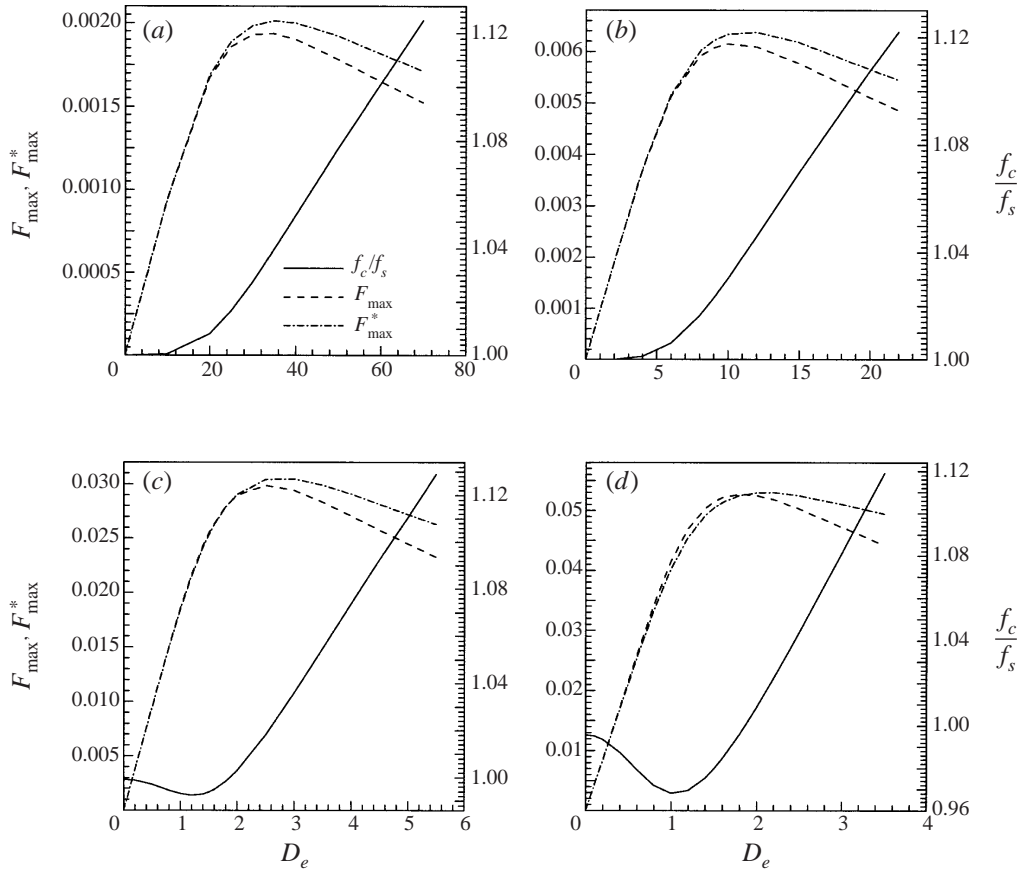


FIGURE 7. The flow resistance  $f_c/f_s$  and secondary volumetric fluxes  $F_{\max}, F_{\max}^*$  versus the Deborah number  $D_e$ ; creeping flow of the UCM fluid. (a)  $\delta = 0.001$ , (b) 0.01, (c) 0.2, (d) 0.5.

| $\delta$ | $D_{e,\max}$ | $\delta^{1/2}D_{e,\max}$ |
|----------|--------------|--------------------------|
| 0.001    | 70.0         | 2.21                     |
| 0.01     | 22.0         | 2.20                     |
| 0.2      | 5.5          | 2.46                     |
| 0.5      | 3.5          | 2.47                     |

TABLE 6. Values of the limiting Deborah number of the UCM fluid for various curvature ratios.

satisfies

$$\mathbf{R}(\mathbf{a}_s) = \mathbf{0}, \tag{6.3}$$

and define the perturbation vector as  $\mathbf{b} = \mathbf{a}_s - \mathbf{a}$ , then we can construct a linearized equation as

$$\mathbf{M} \frac{d\mathbf{b}}{dt} + \mathbf{J}(\mathbf{a}_s)\mathbf{b} = \mathbf{0}, \tag{6.4}$$

where  $\mathbf{J}(\mathbf{a}_s)$  is the Jacobi matrix evaluated at  $\mathbf{a}_s$ . The evolution equation (6.4) for the perturbation vector is the basis on which linear stability analyses are usually carried

out. Since  $d\mathbf{b}/dt = -d\mathbf{a}/dt$ , equation (6.4) is equivalent to

$$\mathbf{J}(\mathbf{a}_s)\mathbf{b} = -\mathbf{R}(\mathbf{a}),$$

which is a quasi-Newton iteration algorithm with the Jacobi matrix held constant. Because we have not done temporal calculations and the disturbances in the process of Deborah number augmentation are not random, we recognize that the limiting Deborah numbers achievable under Newton iterations are not equivalent to those obtained with (6.4), at the onset of elastic instabilities, but the subtle relation between them is certainly worth further investigation.

## 7. Impact of the second normal stress difference

In the creeping flow of viscoelastic fluids, the driving force for the secondary flow in a curved pipe is the hoop stress formed by the first normal stress difference ( $N_1$ ) and the streamline curvature. It is essentially the same effect that drives flow instability in a curved channel where the stabilizing effect of negative second normal-stress difference ( $N_2$ ) was discovered in 1964 by Datta and later noted by Beris *et al.* (1992), and Shaqfeh, Muller & Larson (1992), and was subsequently given a simple physical explanation by Graham (1998) – the tension in the neutral direction resists the deformations that lead to instability. Here we intend to examine the impact of  $N_2$  on the steady flow in curved pipes by considering non-zero  $\mu$  in the equation (2.10). In a simple shear flow with shear rate  $\dot{\gamma}$ , this model predicts a constant viscosity,  $\eta_s + \eta_p$ , and the first and second normal-stress differences as

$$N_1 = 2\eta_p D_e \dot{\gamma}^2, \quad N_2 = -\mu\eta_p D_e \dot{\gamma}^2. \quad (7.1)$$

The ratio of the second to first normal-stress difference is  $N_2/N_1 = -\mu/2$ ; from experimental evidence (e.g. Tanner 2000),  $N_2/N_1 = -0.1$  is a typical value for polymer melts or solutions. Furthermore, let us choose  $\eta_s = 0$  and name this model UCMN<sub>2</sub>, and consider the small curvature ratio  $\delta = 0.01$  and the large curvature ratio  $\delta = 0.2$ .

Figure 8 compares the predictions of the UCM and UCMN<sub>2</sub> models for flow resistances  $f_c/f_s$  and secondary volumetric fluxes  $F_{\max}$ . The negative second normal-stress difference has dramatically attenuated the secondary flows. In the case of  $\delta = 0.01$ , the secondary flow has almost disappeared above  $D_e = 10$  and the drag behaves like that in a Poiseuille flow in a straight pipe. It was observed that very small  $\mu$  makes the computation unstable while for the typical value  $\mu = 0.2$  the computation is more stable; for example, in the case of  $\delta = 0.2$ , the limiting Deborah number for the UCM model is 5.5 while those for the UCMN<sub>2</sub> model with  $\mu = 0.1$  and  $\mu = 0.2$  are 3.0 and 9.0, respectively. This phenomenon parallels the discovery of Graham (1998) about the effect on the elastic instabilities of adding axial flows to a circular Couette flow.

Figure 9 plots the contours of the axial velocity  $u_\psi$ , the pressure  $p$ , and the normal stresses  $S_{\theta\theta}$  and  $S_{\psi\psi}$  of two typical cases. For the small curvature ratio  $\delta = 0.01$  and  $D_e = 20$ , these contours approximate that of Poiseuille flow in a straight pipe for which it is easy to prove that

$$S_{\theta\theta} = \frac{\mu}{2} S_{\psi\psi} \quad \text{and} \quad \frac{\partial p}{\partial r} = -\frac{S_{\theta\theta}}{r}. \quad (7.2)$$

Actually,  $S_{rr}$  is two orders of magnitude less than  $S_{\theta\theta}$  in the computations, thus the stresses  $S_{\psi\psi}$  and  $S_{\theta\theta}$  in the left-hand column of figure 9 represent the first and

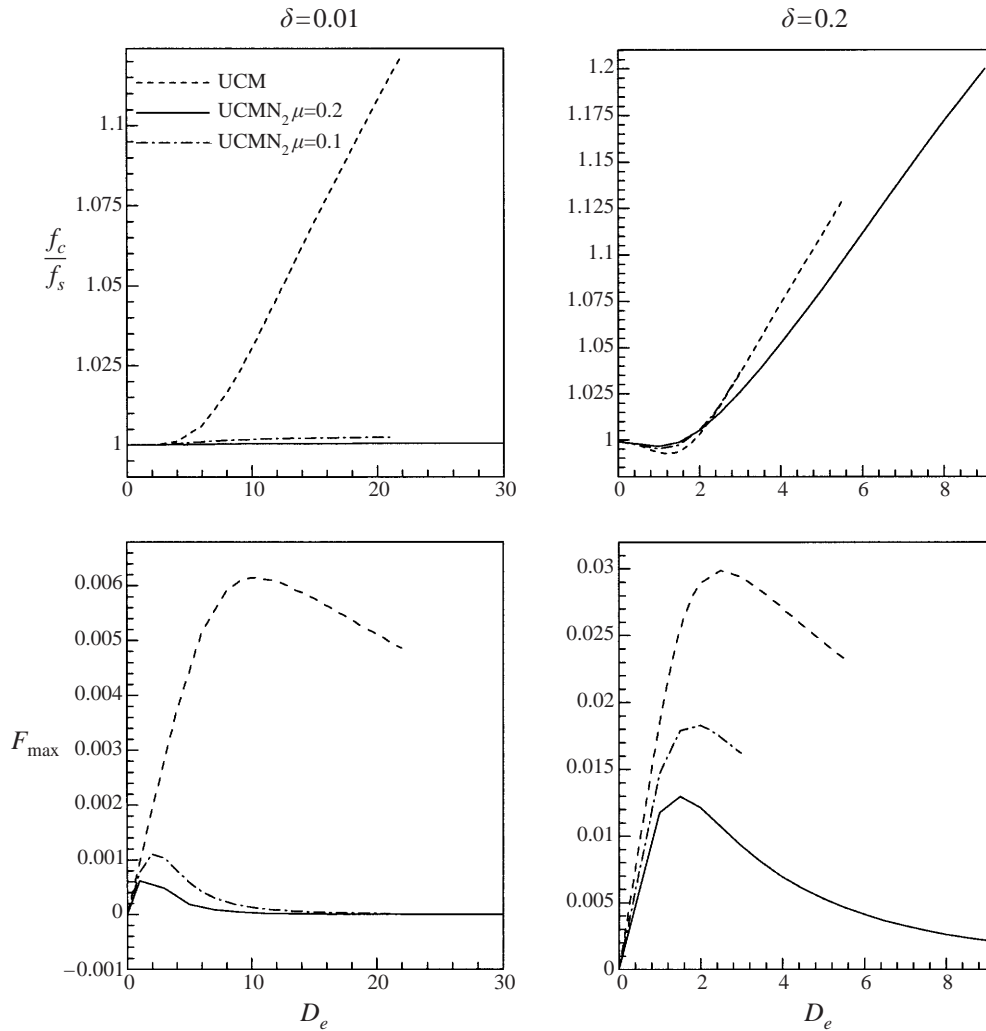


FIGURE 8. The flow resistance  $f_c/f_s$  and secondary volumetric flux  $F_{\max}$  versus the Deborah number  $D_e$  for the UCM and UCMN<sub>2</sub> models.

second normal-stress differences, respectively. For the large curvature ratio  $\delta = 0.2$  and  $D_e = 8$ , the normal stresses  $S_{\theta\theta}$  and  $S_{\psi\psi}$  form boundary layer structures on the outer bend of the wall.

### 8. Inertial flow of viscoelastic fluids

We first consider the inertial flow of Oldroyd-B fluids by setting  $\mu = 0$  in the constitutive equation (2.10). In a simple shear flow with shear rate  $\dot{\gamma}$ , the Oldroyd-B model predicts the constant viscosity  $\eta_s + \eta_p$  and the first normal-stress difference  $N_1$  given by equation (7.1) ( $N_2 = 0$ ). To make the study reasonably focused we fix the relative solvent viscosity at  $\eta_s = 0.5$ . For inertial viscoelastic flows, an elasticity number,  $E_n$ , can be defined to characterize the elastic level with respect to the inertia:

$$E_n = \frac{D_e \eta_p}{R_n} = \frac{\lambda \eta_p^*}{\rho a^2}. \tag{8.1}$$

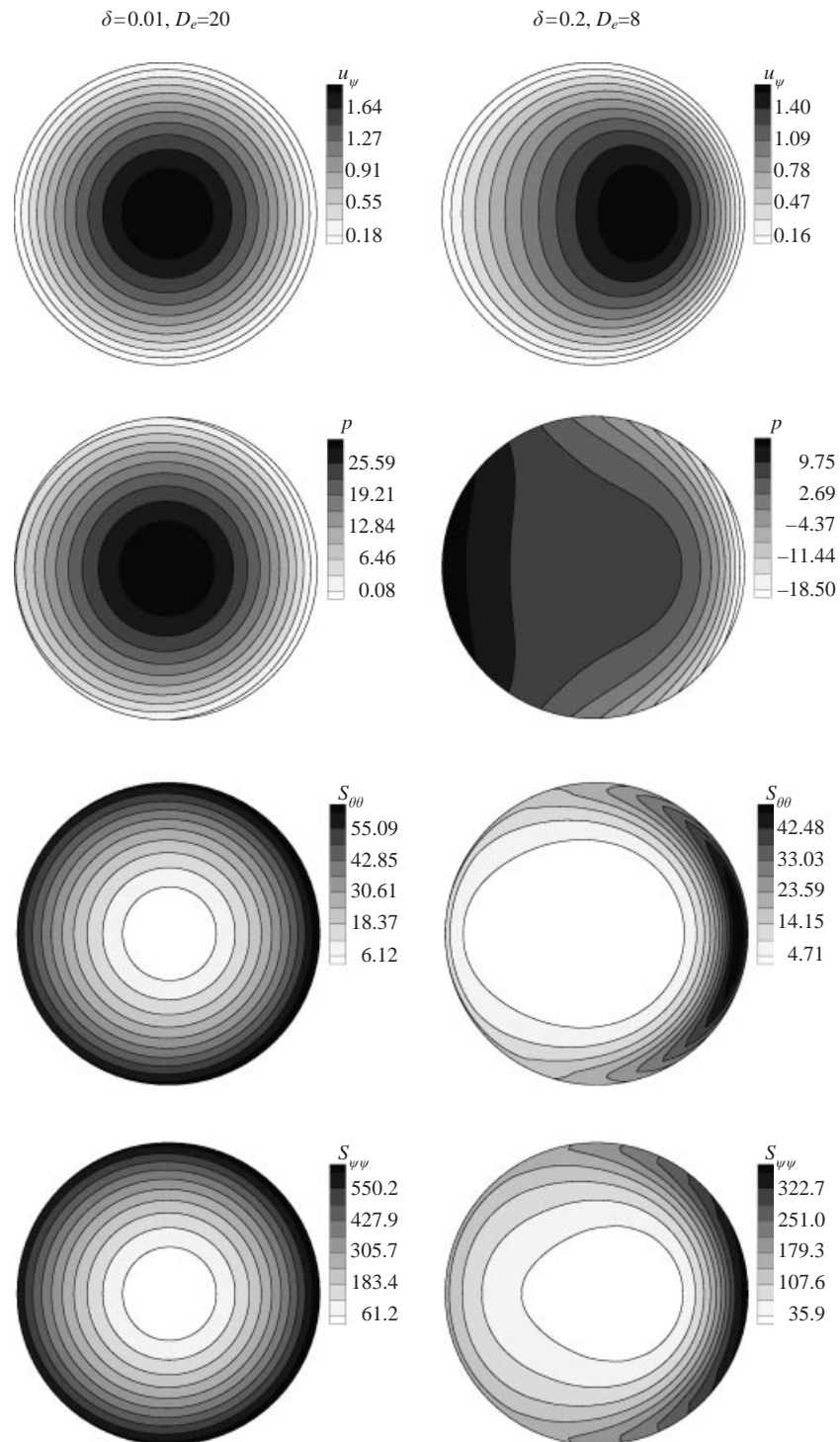


FIGURE 9. Contours of the axial velocity  $u_\psi$ , the pressure  $p$  and the normal stresses  $S_{00}, S_{\psi\psi}$  for the Oldroyd-3-constant fluid with  $\eta_s = 0$  and  $\mu = 0.2$  (UCMN<sub>2</sub> model).

| $\delta$ | $R_n$ | $D_e$ | $f_c/f_s$ | $(f_c/f_s)_R$ | $F_{rms}$            | $ER_t$               | $ER_x$               | $ER_y$               |
|----------|-------|-------|-----------|---------------|----------------------|----------------------|----------------------|----------------------|
| 0.01     | 20.0  | 0.4   | 1.000193  | 1.000194      | $3.3 \times 10^{-4}$ | $3.1 \times 10^{-7}$ | $2.6 \times 10^{-7}$ | $6.2 \times 10^{-6}$ |
| 0.01     | 80.0  | 1.6   | 1.022411  | 1.028247      | $4.9 \times 10^{-2}$ | $4.3 \times 10^{-5}$ | $4.2 \times 10^{-5}$ | $3.4 \times 10^{-5}$ |
| 0.01     | 100.0 | 2.0   | 1.043758  | 1.070371      | $1.0 \times 10^{-1}$ | $1.0 \times 10^{-4}$ | $9.9 \times 10^{-5}$ | $7.9 \times 10^{-5}$ |
| 0.01     | 20.0  | 2.0   | 1.000490  | 1.000490      | $1.5 \times 10^{-3}$ | $1.2 \times 10^{-5}$ | $1.2 \times 10^{-5}$ | $1.6 \times 10^{-3}$ |
| 0.01     | 40.0  | 4.0   | 1.007013  | 1.007369      | $2.5 \times 10^{-2}$ | $8.2 \times 10^{-5}$ | $8.1 \times 10^{-5}$ | $1.8 \times 10^{-3}$ |
| 0.01     | 60.0  | 6.0   | 1.027684  | 1.037906      | $1.1 \times 10^{-1}$ | $3.2 \times 10^{-4}$ | $3.2 \times 10^{-4}$ | $2.7 \times 10^{-3}$ |
| 0.2      | 5.0   | 0.1   | 1.001697  | 1.001685      | $4.4 \times 10^{-3}$ | $1.9 \times 10^{-5}$ | $3.0 \times 10^{-5}$ | $7.1 \times 10^{-5}$ |
| 0.2      | 10.0  | 0.2   | 1.010651  | 1.011257      | $1.7 \times 10^{-2}$ | $1.9 \times 10^{-5}$ | $3.2 \times 10^{-5}$ | $6.9 \times 10^{-5}$ |
| 0.2      | 20.0  | 0.4   | 1.055809  | 1.083957      | $1.0 \times 10^{-1}$ | $1.7 \times 10^{-5}$ | $3.4 \times 10^{-6}$ | $1.1 \times 10^{-4}$ |
| 0.2      | 10.0  | 1.0   | 1.015936  | 1.015167      | $3.3 \times 10^{-2}$ | $2.2 \times 10^{-5}$ | $2.1 \times 10^{-6}$ | $1.9 \times 10^{-3}$ |
| 0.2      | 15.0  | 1.5   | 1.051602  | 1.070664      | $1.4 \times 10^{-1}$ | $2.4 \times 10^{-4}$ | $1.9 \times 10^{-4}$ | $2.5 \times 10^{-3}$ |
| 0.2      | 20.0  | 2.0   | 1.094931  | 1.243765      | $3.4 \times 10^{-1}$ | $7.4 \times 10^{-4}$ | $6.4 \times 10^{-4}$ | $4.4 \times 10^{-3}$ |

TABLE 7. Comparison of the solutions using *PO2* with the perturbation solutions of Robertson & Muller (1996); the inertial flow of the Oldroyd-B fluid.

Note that for a given geometry, the elasticity number is only a function of the fluid properties. Due to the difficulty of reaching high Deborah numbers, we only present the results for the small elasticity numbers,  $E_n = 0.05, 0.01$ .

Table 7 shows that our results for the flow resistance and the stream function agree well with the perturbation solutions of Robertson & Muller (1996) at relatively small Reynolds/Deborah numbers. Figure 10 exhibits the dependence of the flow resistance  $f_c/f_s$  and the secondary volumetric flux  $F_{max}$  on the Reynolds number. The qualitative behaviour of  $f_c/f_s$  and  $F_{max}$  for Oldroyd-B fluid is the same as that for Newtonian fluid. From  $E_n = 0$  to  $E_n = 0.05$ , the influence of the viscoelasticity is to increase the flow resistance and, first enhance the secondary volumetric flux, then after the peak value, reduce it considerably; the behaviour of  $F_{max}^*$  which is not presented here is similar to that of  $F_{max}$ . According to the analysis in the Appendix, in the core region the approximate momentum balance is

$$R_n \frac{u_v^2}{Q} \approx \frac{\partial p}{\partial x} + \frac{S_{\psi v}}{Q}. \tag{8.2}$$

Note that when approaching to the wall, both the larger  $S_{\psi v}$  and smaller  $u_v^2$  are positive influences to strengthen the secondary flow.

Figure 11 plots contours of the pressure and axial velocity  $u_v$  for the case of  $\delta = 0.2$ . It can be seen that for the relatively large elasticity number ( $R_n = 50$  and  $D_e = 5$ ) the distributions of the pressure  $p$  and  $u_v$  show an obvious competing effect of fluid inertia and elasticity (see figures 4, 6), while for the small elasticity number ( $R_n = 200$  and  $D_e = 4$ ) the corresponding distributions are dominated by the fluid inertia.

We checked the maximum Reynolds number for which our Newton iteration algorithm can converge, and found that the limiting Deborah numbers are approximately the same as that for the creeping flow of the UCM fluid. As shown in table 8, the dimensionless parameter  $\delta^{1/2}D_e$  can also be used to characterize the convergence breakdown problem here.

Let us examine the influence of the second normal stress difference on the inertial viscoelastic flow by choosing a typical value  $\mu = 0.2$  in the constitutive equation (2.10).

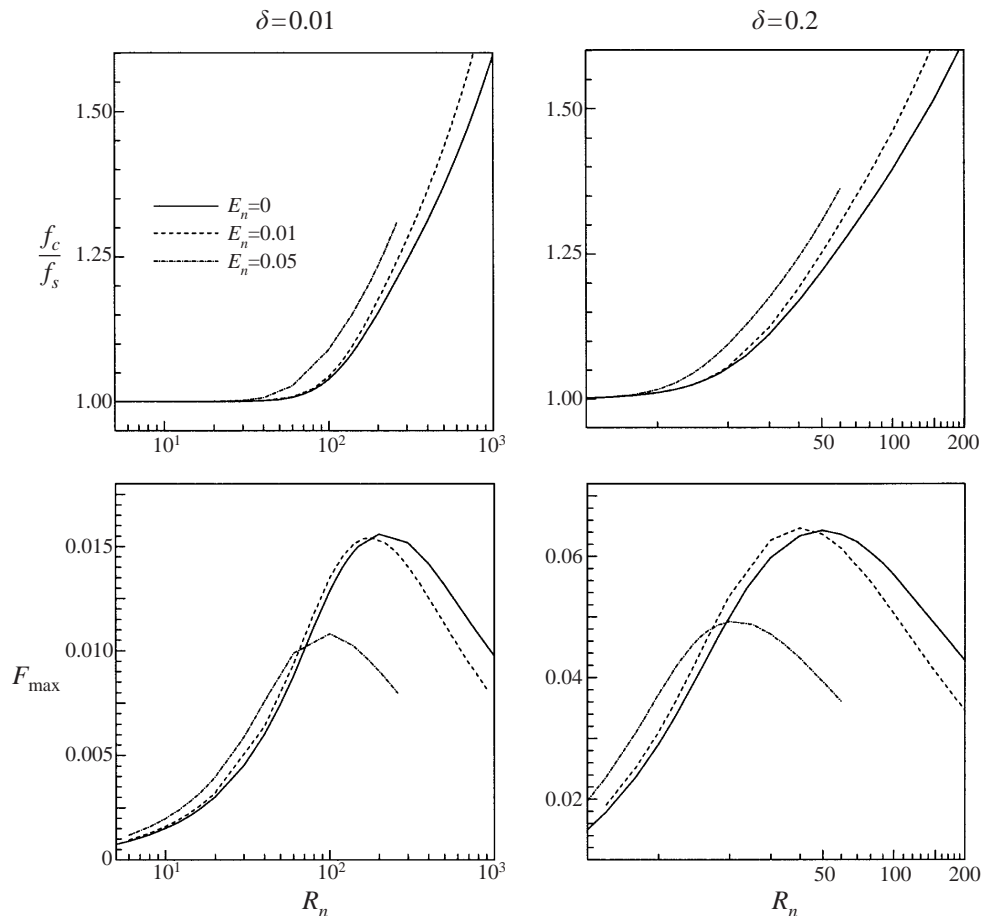


FIGURE 10. The flow resistance  $f_c/f_s$  and secondary volumetric flux  $F_{\max}$  versus the Reynolds number  $R_n$ ; the elasticity number  $E_n = 0$  is Newtonian fluid,  $E_n = 0.01$  and  $0.05$  are Oldroyd-B fluids with  $\eta_s = 0.5$ .

Figure 12 shows the predicted flow resistances  $f_c/f_s$  and the secondary volumetric fluxes  $F_{\max}$  versus the Reynolds number  $R_n$ . As in the case of creeping flow, the second normal-stress difference has dramatically attenuated the secondary flows. In the case of  $\delta = 0.01$  and  $E_n = 0.05$ , the secondary flow has almost disappeared for  $R_n > 100$ . The effect on the flow resistance is different for large and small curvature ratios: in the case of  $\delta = 0.2$ , the flow resistance increases monotonically with increasing elasticity number and is greater than the Newtonian value, while in the case of  $\delta = 0.01$ , for  $R_n > 50$ , the flow resistance decreases with increasing the elasticity number and seems to approach an asymptotic value which is considerably lower than the Newtonian value. This drag reduction is consistent with the experimental observations for dilute polymer solutions with small curvature ratios at low Reynolds numbers (Jones & Davies 1976; Mashelkar & Devarajan 1976). However, the present model seems to lack a mechanism that produces the subsequent considerable drag increases when the Reynolds number further increases, as observed in the experiments. This may be attributed to some shortcomings of the model, especially the quadratic dependence of the normal stress differences on the shear rate, whereas, for example,



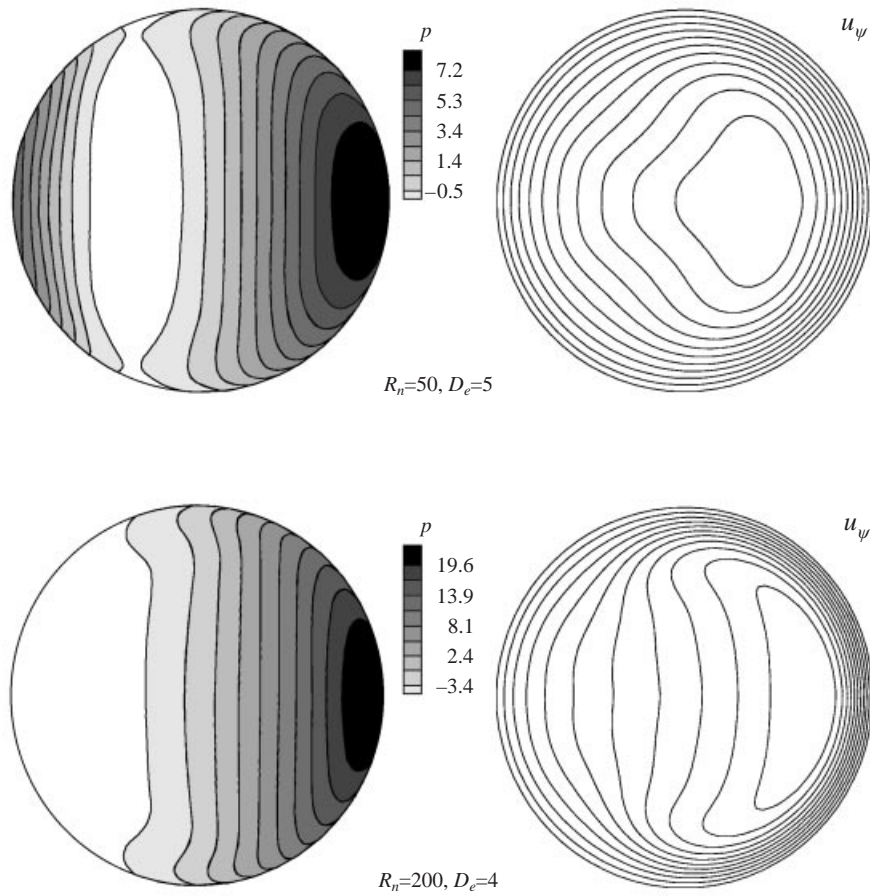


FIGURE 11. Contours of the pressure  $p$  and the axial velocity  $u_\psi$ ; the inertial flow of Oldroyd-B fluid with  $\eta_s = 0.5$  and  $\delta = 0.2$ ; the contour levels are equally divided between the maximum and the minimum.

---

| $\delta$ | $E_n$ | $R_{n,max}$ | $D_{e,max}$ | $\delta^{1/2}D_{e,max}$ |
|----------|-------|-------------|-------------|-------------------------|
| 0.01     | 0.01  | 1200        | 24.0        | 2.4                     |
| 0.01     | 0.05  | 260         | 26.0        | 2.6                     |
| 0.2      | 0.01  | 280         | 5.6         | 2.50                    |
| 0.2      | 0.05  | 60          | 6.0         | 2.68                    |

---

TABLE 8. Values of the limiting Reynolds/Deborah numbers of the Oldroyd-B fluid.

in the experiments of Mashelkar & Devarajan (1976) for dilute polymer solutions, this dependence is approximately linear.

It was observed that the negative second normal-stress difference makes the computation more stable: for example, the upper limit of the Reynolds number for Oldroyd-B fluid with  $\delta = 0.2$  and  $E_n = 0.05$  is 60, while for the Oldroyd-3-constant model with  $\delta = 0.2$ ,  $E_n = 0.05$  and  $\mu = 0.2$  the limit exceeds 200.

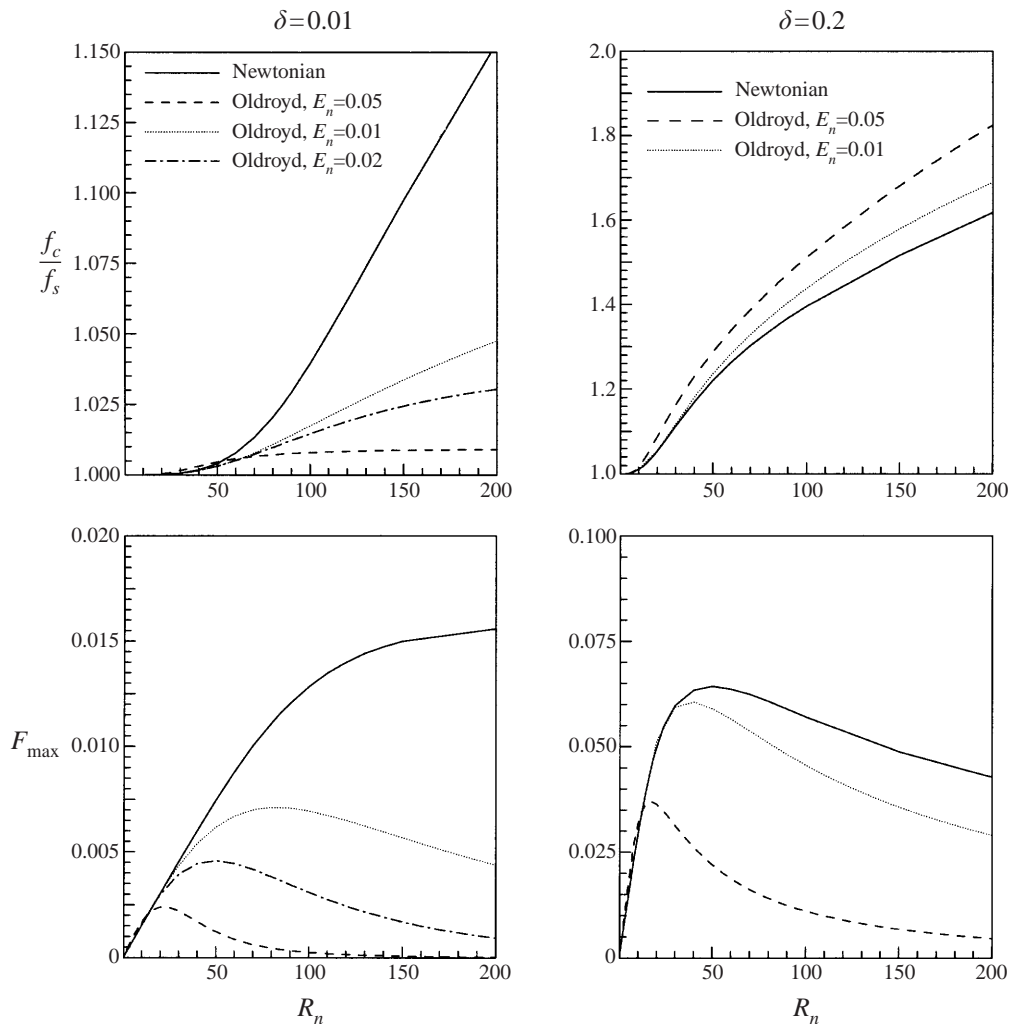


FIGURE 12. The flow resistance  $f_c/f_s$  and secondary volumetric flux  $F_{\max}$  versus the Reynolds number  $R_n$  for Oldroyd-3-constant fluids with  $\eta_s = 0.5$  and  $\mu = 0.2$ .

## 9. Conclusion

From the global torque- and force-balance analysis, we have proposed three criteria to check numerical solutions for the fully developed flow in curved pipes. These criteria have been used to estimate the errors in the  $h$ - $p$  finite element computations for the Newtonian and viscoelastic fluids in this study. We recommend them as the error estimations for any future numerical investigations on this problem.

Our computations of the flow resistance and secondary stream function are in close agreement with the perturbation solutions of Robertson & Muller (1996) in the cases of small Reynolds/Deborah numbers. On the other hand, the numerical solutions can be used to estimate the range of validity of the perturbation solutions. Through the  $h$ - $p$  extension computations and the error estimations, more accurate solutions than those in the previous literature are assured, especially for the large curvature ratios.

Based on our numerical solutions and analysis of the order of magnitude in the governing equations, the mechanism of the secondary flow for fluids with zero second

normal-stress difference can be summarized as follows. For Newtonian flow, the pressure gradient, established essentially by the centrifugal force in the core region, becomes the driving force of the secondary flow near the wall region. For creeping viscoelastic flow, the pressure gradient is essentially balanced by the axial normal stress in the core region; however, near the wall it cannot compete with the large axial normal stress there, which is why viscoelasticity promotes a secondary flow in the same direction as the inertial secondary flow, despite the adverse pressure gradient in the wall region. In the case of inertial viscoelastic flow, when approaching the wall, both the larger axial normal stress and the smaller inertia are positive contributions to increasing the secondary flow.

The maximum stream functions  $F_{\max}$  and  $F_{\max}^*$  have been used to quantify the intensity of the secondary flow; they represent the secondary volumetric flux per unit work consumption and per unit axial volumetric flux, respectively. The qualitative behaviours of these two fluxes are the same for both Newtonian and viscoelastic fluids: they first increase with the Reynolds/Deborah numbers, then decrease. This phenomenon has not been reported in the literature and we expect it to be confirmed by future experiments. Obviously, it should be of interest in engineering applications, because the secondary flow is closely related to the heat/mass transfer character of the flow in curved pipes.

The impact of the second normal-stress difference on the flow in curved pipes has been examined: a small negative second normal-stress difference can drastically suppress the secondary flow and in the case of small curvature ratios, makes the flow approximate the corresponding Poiseuille flow in a straight pipe. For the UCM or Oldroyd-B models, the first normal-stress difference in the axial flow promotes a secondary flow which gives rise to a tensile stress in the neutral direction; however, the effect of this tensile stress is equivalent to a negative second normal-stress difference, i.e. to suppress the secondary flow. The competition between these two factors may be responsible for the observed increase/decrease behaviour of the viscoelastic secondary flows.

Our work on the steady solutions may provide the base solutions required for elastic instability investigations. Furthermore, the limiting Deborah numbers met for the UCM and Oldroyd-B models were observed to obey the same scaling criterion as proposed by McKinley *et al.* (1996) for elastic instabilities; we present the intriguing problem of the subtle relation between Newton iteration for steady solutions and linear stability analyses.

The drag reduction in creeping flow of UCM fluid with large curvature ratios predicted by our computation is rather interesting: the drag of a viscoelastic flow in a curved pipe can be considerably lower than that in the corresponding straight pipe. For the inertial flow of Oldroyd-B fluid, our computation predicts drag enhancement due to the viscoelasticity. The situation, however, becomes more complicated when a non-zero second normal-stress difference is considered. The Oldroyd-3-constant model predicts that for small curvature ratios, a typical negative second normal-stress differences makes the flow approximate the corresponding Poiseuille flow in a straight pipe, and, consequently, produces large drag reductions compared to Newtonian flow; however, for large curvature ratios, although the secondary flow is also greatly attenuated by the second normal-stress difference, the flow resistance remains considerably higher than for Newtonian flow. The present Oldroyd-3-constant model is still too simple to quantitatively predict the drag behaviour of dilute polymer solutions in the whole range of Reynolds number observed in the experiments (Jones & Davies 1976; Mashelkar & Devarajan 1976). Generally, the first and second normal-

stress differences predicted by the Oldroyd model do not fit the experiments for most polymer solutions; therefore further work on more realistic, carefully calibrated viscoelastic models is needed.

We gratefully acknowledge the support from the Australian Research Council (ARC). Y. R. Fan also acknowledges the support of the National Natural Science Foundation of China. The computations were done on the Sydney Distributed Computing (SyDCom) Laboratory.

### Appendix. Analysis of the order of magnitude for the Oldroyd-B fluid

Owing to the fully developed flow assumption, in the following equations, the terms containing  $\partial/\partial\psi$  have been dropped and we employ the *symbolic* expressions:

$$Q = R + r \cos \theta, \quad (\text{A } 1)$$

$$(\mathbf{u} \cdot \nabla) = u_r \frac{\partial}{\partial r} + u_\theta \frac{\partial}{r \partial \theta}. \quad (\text{A } 2)$$

The components of the strain rate tensor,  $\mathbf{D} = \nabla \mathbf{u} + (\nabla \mathbf{u})^T$ , are

$$\left. \begin{aligned} D_{rr} &= 2 \frac{\partial u_r}{\partial r}; & D_{\theta\theta} &= 2 \left( \frac{\partial u_\theta}{r \partial \theta} + \frac{u_r}{r} \right); & D_{r\theta} &= \left( \frac{\partial u_\theta}{\partial r} + \frac{\partial u_r}{r \partial \theta} - \frac{u_\theta}{r} \right); \\ D_{r\psi} &= \left( \frac{\partial u_\psi}{\partial r} - \frac{u_\psi \cos \theta}{Q} \right); & D_{\theta\psi} &= \left( \frac{\partial u_\psi}{r \partial \theta} + \frac{u_\psi \sin \theta}{Q} \right); \\ D_{\psi\psi} &= 2 \frac{u_r \cos \theta - u_\theta \sin \theta}{Q}. \end{aligned} \right\} \quad (\text{A } 3)$$

The continuity equation is

$$\frac{\partial u_r}{\partial r} + \frac{\partial u_\theta}{r \partial \theta} + \frac{u_r}{r} + \frac{u_r \cos \theta - u_\theta \sin \theta}{Q} = 0. \quad (\text{A } 4)$$

The component forms of the momentum equation are

$$\begin{aligned} R_n \left( (\mathbf{u} \cdot \nabla) u_r - \frac{u_\theta^2}{r} - \frac{u_\psi^2 \cos \theta}{Q} \right) &= -\frac{\partial p}{\partial r} + \frac{\partial \tau_{rr}}{\partial r} + \frac{\partial \tau_{r\theta}}{r \partial \theta} + \frac{\tau_{rr} - \tau_{\theta\theta}}{r} \\ &\quad + \frac{\tau_{rr} \cos \theta - \tau_{r\theta} \sin \theta - \tau_{\psi\psi} \cos \theta}{Q}, \end{aligned} \quad (\text{A } 5)$$

$$\begin{aligned} R_n \left( (\mathbf{u} \cdot \nabla) u_\theta + \frac{u_\theta u_r}{r} + \frac{u_\psi^2 \sin \theta}{Q} \right) &= -\frac{\partial p}{r \partial \theta} + \frac{\partial \tau_{r\theta}}{\partial r} + \frac{\partial \tau_{\theta\theta}}{r \partial \theta} \\ &\quad + \frac{2\tau_{r\theta}}{r} + \frac{\tau_{r\theta} \cos \theta - \tau_{\theta\theta} \sin \theta + \tau_{\psi\psi} \sin \theta}{Q}, \end{aligned} \quad (\text{A } 6)$$

$$\begin{aligned} R_n \left( (\mathbf{u} \cdot \nabla) u_\psi + \frac{u_\psi (u_r \cos \theta - u_\theta \sin \theta)}{Q} \right) &= \frac{-C}{Q} + \frac{\partial \tau_{r\psi}}{\partial r} + \frac{\partial \tau_{\theta\psi}}{r \partial \theta} \\ &\quad + \frac{\tau_{r\psi}}{r} + \frac{2(\tau_{r\psi} \cos \theta - \tau_{\theta\psi} \sin \theta)}{Q}, \end{aligned} \quad (\text{A } 7)$$

where  $\boldsymbol{\tau}$  is the extra tensor, which can be split as

$$\boldsymbol{\tau} = \eta_s \mathbf{D} + \mathbf{S}. \quad (\text{A } 8)$$

For the Oldroyd-B model,  $\mathbf{S}$  obeys the upper-convected Maxwell (UCM) constitutive equation, for which the component forms are

$$S_{rr} + D_e \left( (\mathbf{u} \cdot \nabla) S_{rr} - S_{rr} D_{rr} - 2S_{r\theta} \frac{\partial u_r}{r \partial \theta} \right) = \eta_p D_{rr}, \quad (\text{A } 9)$$

$$S_{\theta\theta} + D_e \left( (\mathbf{u} \cdot \nabla) S_{\theta\theta} - S_{\theta\theta} D_{\theta\theta} - 2S_{r\theta} \left( \frac{\partial u_\theta}{\partial r} - \frac{u_\theta}{r} \right) \right) = \eta_p D_{\theta\theta}, \quad (\text{A } 10)$$

$$S_{r\theta} + D_e \left( (\mathbf{u} \cdot \nabla) S_{r\theta} + S_{r\theta} D_{\psi\psi} / 2 - S_{rr} \left( \frac{\partial u_\theta}{\partial r} - \frac{u_\theta}{r} \right) - S_{\theta\theta} \frac{\partial u_r}{r \partial \theta} \right) = \eta_p D_{r\theta}, \quad (\text{A } 11)$$

$$S_{r\psi} + D_e \left( (\mathbf{u} \cdot \nabla) S_{r\psi} + S_{r\psi} D_{\theta\theta} / 2 - S_{rr} D_{r\psi} - S_{r\theta} D_{\theta\psi} - S_{\theta\psi} \frac{\partial u_r}{r \partial \theta} \right) = \eta_p D_{r\psi}, \quad (\text{A } 12)$$

$$S_{\theta\psi} + D_e \left( (\mathbf{u} \cdot \nabla) S_{\theta\psi} + S_{\theta\psi} D_{rr} / 2 - S_{\theta\theta} D_{\theta\psi} - S_{r\theta} D_{r\psi} - S_{r\psi} \left( \frac{\partial u_\theta}{\partial r} - \frac{u_\theta}{r} \right) \right) = \eta_p D_{\theta\psi}, \quad (\text{A } 13)$$

$$S_{\psi\psi} + D_e \left( (\mathbf{u} \cdot \nabla) S_{\psi\psi} - S_{\psi\psi} D_{\psi\psi} - 2S_{r\psi} D_{r\psi} - 2S_{\theta\psi} D_{\theta\psi} \right) = \eta_p D_{\psi\psi}. \quad (\text{A } 14)$$

The secondary flow is rather weak in comparison to the axial flow: generally, the velocity components  $u_r, u_\theta$  are two-orders of magnitude smaller than the component  $u_\psi$ . The following order of magnitude approximations will be made:

$$u_r, u_\theta \sim O(\varepsilon) \ll 1, \quad u_\psi \sim O(1). \quad (\text{A } 15)$$

If we consider the region far from the wall we can assume that

$$\frac{\partial}{\partial r}, \frac{\partial}{\partial \theta} \sim O(1). \quad (\text{A } 16)$$

Thus from (A 3) it follows that

$$D_{rr}, D_{\theta\theta}, D_{r\theta}, D_{\psi\psi} \sim O(\varepsilon), \quad D_{r\psi}, D_{\theta\psi} \sim O(1). \quad (\text{A } 17)$$

Notice that (A 9), (A 10) and (A 11) are self-contained in the sense that they contain no axial components of the velocity and stress; it is thus not difficult to show that

$$S_{rr}, S_{\theta\theta}, S_{r\theta} \sim O(\varepsilon). \quad (\text{A } 18)$$

From (A 12) and (A 13), the leading order of  $S_{r\psi}$  and  $S_{\theta\psi}$  can be expressed as

$$S_{r\psi} \approx \eta_p \left( \frac{\partial u_\psi}{\partial r} - \frac{u_\psi \cos \theta}{Q} \right) + O(\varepsilon), \quad S_{\theta\psi} \approx \eta_p \left( \frac{\partial u_\psi}{r \partial \theta} + \frac{u_\psi \sin \theta}{Q} \right) + O(\varepsilon), \quad (\text{A } 19)$$

then from (A 14),  $S_{\psi\psi}$  is estimated as

$$S_{\psi\psi} \approx 2D_e \eta_p \left[ \left( \frac{\partial u_\psi}{\partial r} - \frac{u_\psi \cos \theta}{Q} \right)^2 + \left( \frac{\partial u_\psi}{r \partial \theta} + \frac{u_\psi \sin \theta}{Q} \right)^2 \right] + O(\varepsilon). \quad (\text{A } 20)$$

Combining relations (A 15) to (A 20), the momentum balance in the  $r$ - and  $\theta$ -directions

can be reduced to

$$-R_n \frac{u_\psi^2 \cos \theta}{Q} \approx -\frac{\partial p}{\partial r} - \frac{S_{\psi\psi} \cos \theta}{Q} \quad (\text{A } 21)$$

and

$$R_n \frac{u_\psi^2 \sin \theta}{Q} \approx -\frac{\partial p}{r \partial \theta} + \frac{S_{\psi\psi} \sin \theta}{Q}, \quad (\text{A } 22)$$

which gives rise to the balance in the  $x$ -direction specified in figure 1 as

$$R_n \frac{u_\psi^2}{Q} \approx \frac{\partial p}{\partial x} + \frac{S_{\psi\psi}}{Q}. \quad (\text{A } 23)$$

Notice that we do not invoke the small curvature ratio assumption in the present analysis and the key consequence is that, in the core region ( $u_r, u_\theta \ll u_\psi$ ), the fluid inertia and the axial normal stress are two competitive forces in establishing the pressure gradient or, in other words, the cross-sectional momentum balance is roughly achieved by these three factors.

#### REFERENCES

- AUSTIN, L. R. & SEADER, J. D. 1973 Fully developed viscous flow in coiled circular pipes. *AIChE J.* **19**, 85–94.
- BERGER, S. A., TALBOT, L. & YAO, L. S. 1983 Flow in curved pipes. *Ann. Rev. Fluid Mech.* **15**, 461–512.
- BERIS, A. N., AVGOUSTI, M. & SOUVALIOTIS, A. 1992 Spectral calculations of viscoelastic flows: evaluation of the Giesekus constitutive equation in model flow problem. *J. Non-Newtonian Fluid Mech.* **44**, 197–228.
- BOWEN, P. J., DAVIES, A. R. & WALTERS, K. 1991 On viscoelastic effects in swirling flows. *J. Non-Newtonian Fluid Mech.* **38**, 113–126.
- BROOKS, A. N. & HUGHES, T. J. R. 1982 Streamline upwind Petrov-Galerkin method for convection dominated flows with particular emphasis on the incompressible Navier-Stokes equation. *Comput. Meth. Appl. Mech. Engng* **32**, 199–259.
- DASKOPOULOS, P. & LENHOFF, A. M. 1989 Flow in curved ducts: bifurcation structure for stationary ducts. *J. Fluid Mech.* **203**, 125–148.
- DATTA, S. K. 1964 Note on the stability of an elasticoviscous liquid in Couette flow. *Phys. Fluids* **7**, 1915–1919.
- DEAN, W. R. 1927 Note on the motion of fluid in a curved pipe. *Phil. Mag.* **4**, 208–223.
- DEAN, W. R. 1928 The stream-line motion of fluid in a curved pipe. *Phil. Mag.* **5**, 673–695.
- DENNIS, S. C. R. 1980 Calculation of the steady flow through a curved tube using a new finite-difference method. *J. Fluid Mech.* **99**, 449–467.
- DENNIS, S. C. R. & NG, M. 1982 Dual solutions for steady laminar flow through a curved tube. *Q. J. Mech. Appl. Maths* **35**, 305–324.
- DENNIS, S. C. R. & RILEY, N. 1991 On the fully developed flow in a curved pipe at large Dean number. *Proc. R. Soc. Lond. A* **434**, 473–478.
- FAN, Y. R. & CROCHET, M. J. 1995 High-order finite element methods for steady viscoelastic flows. *J. Non-Newtonian Fluid Mech.* **57**, 283–311.
- FAN, Y. R., TANNER, R. I. & PHAN-THIEN, N. 1999 Galerkin/least-square finite element methods for steady viscoelastic flows. *J. Non-Newtonian Fluid Mech.* **84**, 233–256.
- GRAHAM, M. D. 1998 Effect of axialflow on viscoelastic Taylor-Couette instability. *J. Fluid Mech.* **360**, 341–374.
- GUÉNÉTTE, R. & FORTIN, M. 1995 A new mixed finite element method for computing viscoelastic flows. *J. Non-Newtonian Fluid Mech.* **60**, 27–52.
- HUGHES, T. J. R., FRANCA, L. P. & HUBLERT, G. M. 1989 A new finite element formulation for computational fluid dynamics: VIII. the Galerkin/least-square method for advective-diffusive equations. *Comput. Meth. Appl. Mech. Engng* **73**, 173–189.

- ITO, H. 1969 Laminar flow in curved pipes. *Z. Angew. Math. Mech.* **49**, 653–663.
- JONES, W. M. & DAVIES, O. H. 1976 The flow of dilute aqueous solutions of macromolecules in various geometries: III. Bent pipes and porous materials. *J. Phys. D: Appl. Phys.* **9**, 753–770.
- JONES, S. W., THOMAS, O. M. & AREF, H. 1989 Chaotic advection by laminar flow in a twisted pipe. *J. Fluid Mech.* **209**, 335–357.
- JOO, Y. L. & SHAGFEH, E. S. G. 1994 Observations of purely elastic instabilities in the Taylor-Dean flow of a Boger fluid. *J. Fluid Mech.* **262**, 27–73.
- LARSON, R. G., SHAQFEH, E. S. G. & MULLER, S. J. 1990 A purely elastic instability in Taylor-Couette flow. *J. Fluid Mech.* **218**, 573–600.
- MASHELKAR, R. A. & DEVARAJAN, G. V. 1976 Secondary flows of non-Newtonian fluids: Part I – laminar boundary layer flow of a generalized non-Newtonian fluid in a coiled tube, Part II – frictional losses in laminar flow of purely viscous and viscoelastic fluids through coiled tubes. *Trans. Inst. Chem. Engrs* **54**, 100–114.
- MCKINLEY, G. H., PAKDEL, P. & OZTEKIN, A. 1996 Rheological and geometrical scaling of purely elastic flow instabilities. *J. Non-Newtonian Fluid Mech.* **67**, 19–47.
- NANDAKUMAR, K. & MASLIYAH, J. H. 1982 Bifurcation in steady laminar flow through curved tubes. *J. Fluid Mech.* **119**, 475–490.
- NUNGE, R. J. & LIN, T. S. 1973 Laminar flow in strongly curved tubes. *AIChE J.* **19**, 1280–1281.
- PHAN-THIEN, N. & HUILGOL, R. R. 1985 On the stability of the torsional flow of a class of Oldroyd-type fluids. *Rheol. Acta* **24**, 551–555.
- RAMANAN, V. V., KUMAR, K. A. & GRAHAM, M. D. 2000 Stability of viscoelastic shear flows subjected to steady or oscillatory transverse flow. *J. Fluid Mech.* **379**, 255–277.
- ROBERTSON, A. M. & MULLER, S. J. 1996 Flow of Oldroyd-B fluids in curved pipes of circular and annular cross-section. *Intl J. Non-Linear Mech.* **31**, 1–20.
- SHAQFEH, E. S. G. 1996 Purely elastic instabilities in viscometric flows. *Ann. Rev. Fluid Mech.* **28**, 129–185.
- SHAQFEH, E. S. G., MULLER, S. J. & LARSON, R. G. 1992 The effects of gap width and dilute solution properties on the viscoelastic Taylor-Couette instability. *J. Fluid Mech.* **235**, 285–317.
- SOH, W. Y. & BERGER, S. A. 1987 Fully developed flow in a curved pipe of arbitrary curvature ratio. *Intl J. Numer. Meth. Fluids* **7**, 733–755.
- SOUVALIOTIS, A., JANA, S. C. & OTTINO, J. M. 1995 Potentialities and limitations of mixing simulations. *AIChE J.* **41**, 1605–1621.
- SZABO, B. & BABUSKA, I. 1991 *Finite Element Analysis*. John Wiley & Sons.
- TANNER, R. I. 2000 *Engineering Rheology*, Second Edn. Oxford University Press.
- THOMAS, R. H. & WALTERS, K. 1963 On the flow of an elasto-viscous liquid in a curved pipe under a pressure gradient. *J. Fluid Mech.* **16**, 228–242.
- TOPAKOGLU, H. C. 1967 Steady laminar flows of an incompressible viscous fluid in curved pipes. *J. Math. Mech.* **16**, 1321–1337.
- TSANG, H. Y. & JAMES, D. F. 1980 Reduction of secondary motion in curved tubes by polymer additives. *J. Rheol.* **24**, 589–601.
- YANASE, S., GOTO, N. & YAMAMOTO, K. 1989 Dual solutions of the flow through a curved tube. *Fluid Dyn. Res.* **5**, 191–201.